

Comparing 1-year GUMICS–4 simulations of the Terrestrial Magnetosphere with Cluster Measurements

G. Facskó^{1,2,3}, D. G. Sibeck², I. Honkonen⁴, J. Bór⁵, G. Farinas Perez^{2,3*},
A. Tímár¹, Y. Y. Shprits^{6,7}, L. Degener^{4†}, P. Peitso^{8‡}, E. I. Tanskanen⁸,
C. R. Anekallu⁹, J. Kalmár⁵, S. Szalai^{5,10}, Á. Kis⁵, V. Wesztergom⁵,
N. A. Aseev^{6,7}, Á. Madár^{1,11}

¹Wigner Research Centre for Physics, Budapest, Hungary

²NASA Goddard Space Flight Center, Greenbelt, Maryland, USA

³the Catholic University of America, Washington DC, USA

⁴Finnish Meteorological Institute, Helsinki, Finland

⁵Research Centre for Astronomy and Earth Sciences, Sopron, Hungary

⁶Helmholtz Centre Potsdam, GFZ German Research Centre for Geosciences, Potsdam, Germany

⁷Institute for Physics and Astronomy, University of Potsdam, Potsdam, Germany

⁸Aalto University, School of Electrical Engineering, Espoo, Finland

⁹UCL Department of Space & Climate Physics, Mullard Space Science Laboratory, Dorking, UK

¹⁰University of Miskolc, Department of Geophysics, Miskolc, Hungary

¹¹Eötvös Loránd University, Doctoral School of Physics, Budapest, Hungary

Key Points:

- The GUMICS–4 code provides realistic ion plasma moments and magnetic field in the solar wind and the outer magnetosheath.
- The code [...] predicts [...] realistic bow shock locations [...].
- An inner magnetosphere model should be added to the code to increase the accuracy of the simulation in inner magnetosphere.

*Now at University of Miami, Electrical and Computer Engineering Department, Miami, Florida, USA

†Now private individual, Hannover, Germany

‡Now at Aurora Propulsion Technologies, Espoo, Finland

Corresponding author: Gábor Facskó, facsko.gabor@wigner.hu

24 **Abstract**

25 We compare the predictions of the GUMICS-4 global magnetohydrodynamic
 26 model for the interaction of the solar wind with the Earth's magnetosphere
 27 to Cluster-3 measurements over for one year, from January 29, 2002, to Febru-
 28 ary 2, 2003. In particular, we compare [...] the north/south component of
 29 the magnetic field (B_z), the component of the velocity along the Sun-Earth
 30 line (V_x), and the plasma density as determined from a top hat plasma spec-
 31 trometer and the spacecraft's potential. We select intervals in the solar wind, the
 32 magnetosheath and the magnetosphere where these instruments [...] provided good qual-
 33 ity data and the model correctly predicts the region in which the spacecraft is
 34 located. We determine the location of the bow shock, the magnetopause and, the neu-
 35 tral sheet from the spacecraft measurements and compare their locations to those pre-
 36 dicted by the simulation.

37 The GUMICS-4 model provides quite good results in the solar wind however its
 38 accuracy is worse in the magnetosheath. The simulation results are not realistic in the
 39 magnetosphere. The bow shock location is predicted well however the magnetopause lo-
 40 cation is less accurate. The neutral sheet positions are located quite well thanks to the
 41 special solar wind conditions. [...]

42 **1 Introduction**

43 One of the most cost-effective way to study the interaction of the solar wind with
 44 planetary magnetospheres (or predict the conditions in near-Earth space) is modeling
 45 this complex system using a [...] magnetohydrodynamic (MHD) code. In the past,
 46 several [...] parallelized [...] codes were developed, which are used and applied to fore-
 47 cast the cosmic environment of the Earth; such as the Lyon-Fedder-Mobarry [LFM; Lyon
 48 et al., 2004] code, the Grid Agnostic MHD for Extended Research Applications
 49 [GAMERA; Zhang et al., 2019], the Open Geospace General Circulation Model [OpenG-
 50 GCM; Raeder et al., 2008], the Block-Adaptive-Tree-Solarwind-Roe-Upwind-Scheme [BATS-
 51 R-US; Powell et al., 1999; Tóth et al., 2012]. In Europe only three global MHD codes
 52 were developed: the Grand Unified Magnetosphere–Ionosphere Coupling Simulation [GUMICS-4;
 53 Janhunen et al., 2012], the Computational Object Oriented Libraries for Fluid Dynam-
 54 ics [COOLFluiD; Lani et al., 2012] and the 3D resistive magnetohydrodynamic code Gor-
 55 gon [Chittenden et al., 2004; Ciardi et al., 2007]. The COOLFluiD is a general-purpose

plasma simulation tool. The Gorgon code was developed **to study** high energy, collisional plasma interactions and has been adapted to simulate planetary magnetospheres and their interaction with the solar wind [Mejnertsen *et al.*, 2016, 2018]. **Neither Gorgon nor COOLfluid have an ionospheric solver.** [...] **Almost all of** these codes are available at the Community Coordinated Modelling Center (CCMC; <http://ccmc.gsfc.nasa.gov/>) hosted by the NASA Goddard Space Flight Center (GSFC) **or** the Virtual Space Weather Modelling Centre (VSWMC; <http://swe.ssa.esa.int/web/guest/kul-cmpa-federated>; **re-**
quires registration for the European Space Agency (ESA) Space Situational Awareness (SSA) Space Weather (SWE) portal) hosted by the KU Leuven [Poedts *et al.*, 2020]. A comparison of the simulation results **with** spacecraft and ground-based measurements is necessary to understand the abilities and features of the developed tools. A statistical study using long term global MHD runs for validation [...] of the codes seems **is needed**. Because [...] providing long simulations **are** costly and time consuming [...], only a few studies **have been done**, **almost all for periods much less than a year except Liemohn *et al.* [2018]**.

Guild et al. [2008a,b] launched two months of LFM runs and compared the plasma sheet properties in the simulated tail with the statistical properties of six years Geotail magnetic field and plasma observations [Kokubun *et al.*, 1994; Mukai *et al.*, 1994]. The LFM successfully reproduced the global features of the global plasma sheet in **a** statistical sense. However, there were some differences. The **sheet** was too cold, too dense and the bulk flow was faster than the observed plasma sheet [**Kokubun et al., 1994; Mukai et al., 1994**]. The LFM overestimated the ionospheric transpolar potential. The transpolar potential correlated with the speed of the plasma sheet flows. Equatorial maps of density, thermal pressure, thermal energy and, velocity were compared. The LFM overestimated the plasma sheet density close to the Earth, the temperature by a factor of ~ 3 **and** the global average flow speed by a factor of ~ 2 . The LFM reproduced many of the climatological features of the Geotail data set. The low-resolution model underestimated the occurrence of the fast earthward and tailward flows. Increasing the simulation resolution resulted in the development of fast, busty flows. **These flows influenced the statistics and contributed to a better agreement between simulations and observations.**

Zhang et al. [2011] [...] studied the statistics of magnetosphere-ionosphere (MI) coupling **using *Guild et al.* [2008a]'s LFM simulation above**. The polar cap po-

tential and the field aligned currents (FAC), the downward Poynting flux and, the vorticity of the ionospheric convection were compared with observed statistical averages and the Weimer05 empirical model [Weimer, 2005]. The comparisons showed that the LFM model produced quite accurate average distributions of the Region 1 (R1) and Region 2 (R2) currents. The ionospheric **R2** currents in the MHD simulation seemed to **originate** from the diamagnetic ring current. The average LFM **R1** and **R2** currents were **small** compared with the values from the Weimer05 model. The average **Cross Polar Cap Potential (CPCP)** was higher in the LFM simulation than the measurements of the SuperDARN and the Weimer05 model. The average convection pattern was quite symmetric in the LFM simulation ~~against~~ the SuperDARN measurements and the Weimer05 model. The SuperDARN measurements and the Weimer05 model had **a** dawn-dusk asymmetry. In the LFM model, more Poynting flux flowed into the polar region ionosphere than in the Weimer05 model. ~~It was the~~ consequence of the larger CPCP in the LFM simulation. The larger CPCP allowed **a** higher electric field in the polar region. The statistical dependence of the high-latitude convection patterns on Interplanetary Magnetic Field (IMF) clock angle was similar to the SuperDARN measurements [Sofko *et al.*, 1995] and the Weimer05 model. The average ionospheric field-aligned vorticity showed good agreement on the dayside. However, the LFM model gave **a** larger nightside vorticity than SuperDARN measurements because the Pedersen conductance on the night side ionosphere was too low.

Wiltberger et al. [2017] studied the structure of [...] high latitude field-aligned current patterns using three resolutions of the LFM global MHD code and the Weimer05 empirical model [Weimer, 2005]. The studied period was a month-long and contained two high-speed streams. Generally, the patterns agreed well with results obtained from the Weimer05 computing. As the resolution of the simulations increased, the currents became more intense and narrow. The ratio of the Region 1 (R1), the Region 2 (R2) currents and, the R1/R2 ratio increased when the simulation resolution increases. However, both the R1 and R2 currents were smaller than the predictions of the Weimer05 model. This effect led to a better agreement of the LFM simulation results with the Weimer 2005 model results. The CPCP pattern became concentrated in higher latitudes because of the stronger R2 currents. The relationship of the CPCP and the R1 looked evident at **a** higher resolution of the simulation. The LFM simulation could have reproduced the statistical features of the field-aligned current (FAC) patterns.

122 *Hajducek et al.* [2017] simulated the month (~~January, 2005~~) using the Space Weather
 123 Modelling Framework [SWMF; *Tóth et al.*, 2005] and the OMNI solar wind data (<https://omniweb.gsfc.nasa.gov/>)
 124 as input. The simulations were compiled with and without an inner magnetosphere model
 125 and using two different grid resolutions. The model was very good in predicting the ring
 126 currents [...] [SYM-H; <http://wdc.kugi.kyoto-u.ac.jp/aeasy/asy.pdf>; *Iyemori*, 1990]. The
 127 K_p index (that measures the general magnetospheric convention and the auroral currents
 128 [*Bartels et al.*, 1939; *Rostoker*, 1972; *Thomsen*, 2004]) was predicted well during storms
 129 however the index was overestimated during quiet periods. The AL index (that de-
 130 scribes the westward electrojet of the surface magnetic field introduced by *Davis and Sug-*
 131 *iura* [1966]) was predicted reasonably well on average. However the model reached the
 132 highest negative AL value less often it was reached in the observations because the
 133 model captured the structure of the auroral zone currents poorly. The overpredicting of
 134 K_p index during quiet times might have had the same reason because that index was also
 135 sensitive to auroral zone dynamics. The SWMF usually overpredicted the CPCP. These
 136 results were not sensitive to grid resolutions, with the exception of the AL index,
 137 which reached the highest negative value more often when the grid resolution was higher.
 138 Switching off of the inner magnetosphere model had a negative effect on the accuracy
 139 of all quantities mentioned above, except the CPCP.

140 In this paper, the Cluster SC3 measurements are compared directly to a previously
 141 made 1-year long GUMICS–4 simulation in the solar wind, magnetosheath and the mag-
 142 netosphere along the Cluster SC3 orbit saved from the simulation results and measured
 143 by the spacecraft [Facskó et al., 2016]. In this paper these parameters, namely the
 144 B_z , the north/south component of the magnetic field in GSE coordinates, the
 145 solar wind velocity GSE X component (V_x) and the solar wind density n are
 146 compared to the Cluster SC3 measurements as well as the location of the bow
 147 shock, magnetopause and the neutral sheet. These parameters are selected
 148 because [...] B_z controls the magnetosphere, [...] V_x is the main component
 149 of the solar wind velocity [...] and [...] n is the ion plasma momentum that
 150 is the easiest to calculate; furthermore more instruments could determine it
 151 (see Section 2.2). The structure of this paper is as follows. Section 2 describes the GUMICS–4
 152 code, the 1-year simulation and the considered measurements of the Cluster space
 153 mission. Section 3 gives comparisons between the simulations and observations. Results
 154 of the comparison are discussed in Section 4. Finally, Section 5 contains the conclusions.

155 **2 The GUMICS–4 products and Cluster measurements**

156 Here we use two [...] very different [...] time series. The first type is derived from
 157 a previously 1-year **run of the GUMICS–4 simulation** [Facsikó *et al.*, 2016]. The sec-
 158 ond **time series were** measured by the magnetometer, ion plasma and electric field in-
 159 struments of the Cluster reference spacecraft.

160 **2.1 The GUMICS–4 code**

161 The GUMICS–4 has two coupled simulation domains, the magnetospheric domain
 162 outside of $3.7 R_E$ radius **sphere** around the Earth and a coupled ionosphere **module**
 163 **containing 2D height-integrated model of ionosphere**. The GUMICS–4 is not a
 164 parallel code however it **has been** extensively used ~~for~~ studying the energy propagation
 165 ~~processes~~ from the solar wind to the magnetosphere through the magnetopause and other
 166 features [Janhunen *et al.*, 2012, see the references therein]. The code has also been ap-
 167 plied **to study** forced reconnection in the tail [Vörös *et al.*, 2014]. Recently, **several**
 168 **hundred** synthetic two hours duration GUMICS–4 simulation **runs** were made to com-
 169 pare the simulation results to empirical formulas [Gordeev *et al.*, 2013]. The agreement
 170 was quite **good in general, but** the diameter of the magnetopause [...] in the sim-
 171 **ulation deviated significantly from** observations in the tail. The [...] GUMICS–4
 172 **simulation magnetotail** was smaller than ~~what the~~ spacecraft observed ~~and measured~~.
 173 A 1-year long simulation was made using the GUMICS–4 code [Facsikó *et al.*, 2016]. Ju-
 174 usola *et al.* [2014] compared the ionospheric currents, fields and the [...] CPCP in the
 175 **simulation to observations from the** Super Dual Auroral Radar Network (SuperDARN)
 176 radars [Greenwald *et al.*, 1995] and CHAMP spacecraft [Reigber *et al.*, 2002] field aligned
 177 currents (FAC) ~~measurements~~ [Juusola *et al.*, 2007; Ritter *et al.*, 2004]. The [...] CPCP,
 178 [...] the FAC and other currents could not be reproduced properly. ~~The~~ possible cause
 179 of this **poor** agreement could be ~~due to low resolution in inner magnetosphere~~
 180 **and/or** the lack of **an** inner magnetosphere model **incorporating the physics in this**
 181 **region**. This **hypothesis** is supported by the result of Haiducek *et al.* [2017]. Haiducek
 182 *et al.* simulated only a month-long period using a different spatial resolution and [...]
 183 tested the code **with** the inner magnetosphere model of the SWMF **switched off** for
 184 a special run. This run without **an** inner magnetosphere model made it clear that only
 185 the CPCP parameter of the simulation agreed quite well with the measurements. This
 186 fact explained why the agreement between the Cluster SC3 and the GUMICS-4 simu-

lations was so good as described by *Lakka et al.* [2018a,b] based on the CPCP in GUMICS–4 simulations. *Kallio and Facskó* [2015] determined **plasma and magnetic field** parameters along the **lunar** orbit **from** the *Facskó et al.* [2016]’s global MHD simulations. The [...] parameters differed significantly in the **geotail** **indicating a need for** future studies. *Facskó et al.* [2016] determined the footprint of [...] Cluster SC3 using the 1-year simulation and the Tsyganenko T96 empirical model [*Tsyganenko*, 1995]. [...] The agreement of the footprint **was** better in the Northern Hemisphere. The GUMICS–4 tail **was** shorter in the simulations than the observations. [...]

A 1-year global MHD simulation was produced with the GUMICS–4 code using the OMNI solar wind data from January 29, 2002, to February 2, 2003, as input [*Facskó et al.*, 2016]. The creation and analysis of the simulation were based on a work package of the European Cluster Assimilation Technology (ECLAT) project (https://cordis.europa.eu/result/rcn/165813_en.html; <http://www.eclat-project.eu/>). The GUMICS-4 is a serial code [*Janhunen et al.*, 2012] hence the 1-year simulation was made in 1860 independent runs. This interval covered 155 Cluster SC3 orbits and each orbit lasted 57 hours. The FMI supercomputer **at the time** had 12 **cores** on each node hence the 57 hours were divided into 4.7 hours simulation time with one hour initialisation period. Each **sub-interval** used its own **individual** average Geocentric Solar Ecliptic (GSE) IMF magnetic field X component B_x component and dipole tilt angle. All data gaps **in the solar wind were interpolated linearly**. If the data gap of the input file was at the beginning (or the end) **of the** interval **then** the first (or last) good data **from** the input file was used to fill the gap. The initialization of each **simulation run** was made using constant values. These values were the first valid data of the input file repeated 60 times (60 minutes) in the input file of the sub-interval. The simulation results were saved [...] every five minutes. Various simulation parameters, for example, the density, particle density, temperature, magnetic field, solar wind velocity (29 different quantities) were saved from the simulation results along the Cluster reference spacecraft’s **orbit** in the GSE coordinates. [...]

215 2.2 The Cluster SC3 measurements

The Cluster-II spacecraft of the European Space Agency (ESA) were launched in 2000 **and study the** geospace [...] [*Credland et al.*, 1997; *Escoubet et al.*, 2001]. The four spacecraft form a tetrahedron **in space** however here we use only the measurements

of the reference spacecraft, [...] Cluster SC3. The spacecraft were stabilised [...] and their period is ~ 4 s. Hence, the **intrinsic time** resolution of the plasma instruments is 4 s and we use 4 s averaged magnetic field data. The **highest** resolution of the Cluster FluxGate Magnetometer (FGM) magnetic field instrument is 27 Hz [Balogh *et al.*, 1997, 2001]. The ion plasma data **are** provided by the Cluster Ion Spectrometry (CIS) Hot Ion Analyser (HIA) sub-instrument [Reme *et al.*, 1997; Rème *et al.*, 2001]. The CIS HIA instrument is calibrated using the Waves of HIgh frequency Sounder for Probing the Electron density by Relaxation (WHISPER) wave instrument onboard Cluster [Décréau *et al.*, 2001; Trotignon *et al.*, 2010; Blagau *et al.*, 2013, 2014]. **The results of these calibrations can appear** as sudden non-physical jumps in the CIS HIA data. The CIS HIA had different modes to measure ~~in~~ the solar wind and the magnetosphere. When the instrument switched from **one** mode to another mode ~~it appeared as a~~ non-physical **jumps also appear** in the **measurements** [...]. These features **impair** the accuracy of [...] data **analyses**.

We protect our results from these non-physical jumps [...] using a density determination based on different principles. We use the spacecraft potential of the Electric Field and Wave Experiment [EFW ; Gustafsson *et al.*, 1997, 2001] to determine the electron density. This quantity can be calculated using the empirical density formula

$$n_{EFW} = 200(V_{sc})^{-1.85}, \quad (1)$$

where n_{EFW} is the calculated density and V_{sc} is the Cluster EFW spacecraft potential [Trotignon *et al.*, 2010, 2011]. The EFW and the WHISPER were used for the calibration of the CIS HIA and the Plasma Electron and Current Experiment [PEACE; Johnstone *et al.*, 1997; Fazakerley *et al.*, 2010a,b]. Both instruments were still working onboard all Cluster spacecraft. Their stable operation reduced the number of data **gaps**, and **it** also made the data analysis easier.

3 Comparison of measurements to simulation

The [...] parameters **saved** from the GUMICS–4 simulations and the Cluster SC3 magnetic field, solar wind velocity and, density measurements are compared in **different regions, namely** the solar wind, magnetosheath, and magnetosphere **using** cross-correlation calculation. The **temporal** resolution of the simulated Cluster orbit data is mostly five minutes because the **results of the simulations** are saved [...] every five minutes [Fazakerley *et al.*, 2010a,b].

249 *et al.*, 2016]. However, the time difference between points **can** be more than five min-
 250 utes at the boundary of the subintervals, because the length of **the** simulation intervals
 251 is determined in minutes. To facilitate analysis of the simulation results, all simulation
 252 data were interpolated to a one-minute resolution. This method does not provide ex-
 253 tra information to the cross-correlation calculation. The data gaps are eliminated us-
 254 ing **linear** interpolation [...] and extrapolation when the gap is at the start or the end
 255 of the selected interval. The spin resolution (4 s) of Cluster SC3 magnetic field measure-
 256 ments is averaged over **five** minutes around (± 150 s) the timestamps of the saved data.
Then the averaged data were interpolated to a one-minute resolution to make easier—the correlation calculations.

259 For the correlation calculation, intervals are selected carefully in the solar wind (see
 260 **Section 3.1**), the magnetosheath (see **Section 3.2**), the dayside and the night side mag-
 261 netosphere (see **Section 3.3**). In these intervals, the parameters did not vary a lot and
 262 we **require neither** [...] Cluster **nor** the virtual probe **to cross** any boundaries. To
 263 compare [...] the B_z magnetic field, V_x solar wind speed and the n_{CIS} and the n_{EFW}
 264 curves we [...] cross **correlate** selected intervals. [...] We carefully examine **such** cases
 265 and remove [...] intervals **which are too short for the ± 60 minutes correlation**
 266 **calculation** (shorter than four hours) [...] and large data gaps from the correlation
 267 calculation. [...] Those intervals are also **neglected where** the plasma instrument has
 268 a calibration error or **a change in its recording mode as it moves from the mag-**
 269 **netosphere to solar wind** (for example). The electron density is also calculated using [...]
 270 Equation 1 and [...] correlated [...]. We want to avoid **the** calibration errors and sud-
 271 den non-physical jumps mentioned previously. The **correlation results for the den-**
 272 **sity derived from the electric field potential** results do not differ significantly from
 273 **those for the top hat plasma instrument**, however the **n_{EFW} does not have any**
 274 **mode change** and it is applicable in the magnetosphere too (**against** the CIS HIA instru-
 275 **ment**).

276 3.1 Solar wind

277 We use OMNI IMF and solar wind velocity, density, and temperature data as in-
 278 put **to** the simulation. **There is a reason why we compare parameters in the so-**
 279 **lar wind region in the simulation and the measurements. The IMF X component can-**
 280 **not be given to the GUMICS–4 as input [Janhunen et al., 2012; Fácskó et al., 2016]. How-**

ever, the magnetic field of the solar wind has **an X component** in the simulations. Additionally, ~~the~~ solar wind structure might ~~change~~ from the simulation domain boundary at $+32 R_E$ to the sub-solar point of the terrestrial bow shock where all OMNI data is shifted. Almost the same solar wind **time** intervals are used as in [...] Table 1 of *Facskó et al.* [2016]. The number of these intervals is small because [...] Cluster fleet instruments were calibrated in 2002, just after **launch** (Table 1). Hence we do not have a satisfactory ion plasma data coverage for this year. Additionally, to improve the accuracy of the correlation calculation (see below) we delete ~~the intervals that were too short~~ (shorter than five hours) or the CIS HIA instrument changed its mode. The Cluster fleet is located in the solar wind only from December to May and only for a couple of hours during each orbit near [...] apogee. We double-check whether ~~the~~ Cluster SC3 ~~stays~~ in the solar wind in both the simulation and reality. We also check the omnidirectional CIS HIA ion spectra on the Cluster Science Archive (CSA; <https://www.cosmos.esa.int/web/csa/csds-quicklook-plots>). **The spectra must contain one narrow band in the solar wind region.** Hence ~~17 intervals are left in the solar wind to study~~ (Figure 1).

The selected intervals **occur for** quiet solar wind conditions (Figure 2). The GUMICS-4 simulation results have five minutes~~s~~ resolution and the Cluster SC3 measurements have one minute~~s~~ resolution (Figure 3). The measurements vary significantly. In spite of the quiet conditions the solar wind density often changes and deviates from the simulation. [...] Figure 4c **shows that** both densities deviate significantly. The CIS HIA density ~~deviation is~~ larger as [...] expected **given** the complexity and the large number of working modes of the CIS instrument. The magnetic field and the solar wind velocity fit better. [...] Figure 5a **shows that** the correlation of the magnetic fields is very good; furthermore ~~on~~ Figure 5c, 5e, 5g the correlation of the solar wind velocity and density is excellent (Table 1). The time shift on Figure 5b, Figure 5d, Figure 5f is about five minutes for the magnetic field and the CIS data. On Figure 5h for the EFW data the time shift is **less stable**. It is not **as well** determined as **in case of** the other parameters.

3.2 Magnetosheath

~~The~~ Cluster SC3 spent only a little time in the solar wind from December, 2002 to May, 2003. However, the [...] spacecraft **enters** the magnetosheath each orbit (Figure 6). We selected intervals when the value of the magnetic field is around 25 nT. The field should be fluctuating because of the turbulent **deflected** flow of the **shocked** so-

313 lar wind [...] the **temperature should be greater than that in the solar wind [...]**.
 314 The **velocity should decrease to values ranging from 100-300 km/s**. The density
 315 of the plasma **should increase** and reached **values of 10-20 cm⁻³**. The narrow band
 316 on the omnidirectional CIS HIA ion spectra from the CSA (<https://www.cosmos.esa.int/web/csa/csds-quicklook-plots>) **widens from the solar wind to the magnetosheath**. 15–30 minutes
 317 **from each bow shock** crossing we considered the Cluster SC3 to **have entered** into
 318 the magnetosheath. At the inner **magnetopause boundary of the magnetopause** the
 319 flow speed [...] and the density **drop**. The magnetic field **strength increases** and the
 320 **magnetic field becomes** less turbulent than in the magnetosheath. The wide band **on**
 321 **the** the omnidirectional CIS HIA ion spectra disappears. 15–30 minutes before **the** ap-
 322 **pearance of these indicators of the magnetopause crossing our intervals end**. All inter-
 323 **vals contain large data gaps, non-physical jump in instrument modes [...]** or **lasting**
 324 **less** than four hour are removed. Hence 74 intervals considered in our final selection (Ta-
 325 **ble 2**).

327 All intervals have quiet upstream (or input) solar wind conditions (Figure 7). **Inspite**
 328 **of our selected [...]** magnetic field and [...] plasma parameters and the calculated em-
 329 **pirical density indicate that they vary significantly stronger than in the solar wind in-**
 330 **tervals (Figure 8)**. The deviation **between** the simulated and the observed data is also
 331 larger in this region [...]. The **scatter** plots of the magnetic field, plasma flow speed
 332 and the densities **show that these parameters agree well, but with greater vari-**
 333 **ation than the scatter plots for the solar wind** (Figure 9a, 9b, 9c). The correlation of
 334 the simulated and the observed data is good for the magnetic field (Figure 10a), very
 335 good for the ion plasma moments and the calculated density (Figure 10c, 10e, 10g). The
 336 timeshift of the magnetic field is within five minutes mostly (Figure 10b) however the
 337 timeshift of the ion plasma moments is scattered (Figure 10d, 10f). The timeshift of the
 338 calculated EFW density seems to be more **stable** (Figure 10h). Generally, the GUMICS–4
 339 is less accurate in the magnetosheath **than in the solar wind**. **The modelled mag-**
 340 **netic field is closer to the observations than the modelled plasma parameters**
 341 **are**. The calculated empirical EFW density (n_{EFW}) fits better than the CIS HIA den-
 342 **sity (n_{CIS})**.

343 **3.3 Magnetosphere**

344 To select ~~intervals in the~~ magnetosphere we looked ~~for~~ the CIS HIA **omnidirectional**
 345 ion flux **spectrum**. Where the band of ~~the~~ hot magnetosheath ion ~~population~~ (dis)appeared,
 346 the magnetosphere started/finished. The **plasma** density **decreases toward** zero, the
 347 magnetic field **strength is large**. We ~~left~~ 15–30 min after/before the magnetopause trans-
 348 sition to **identify** magnetosphere **intervals**. This way we found 132 intervals in the mag-
 349 netosphere (Table 3) using Cluster SC3 measurements. [...] Cluster SC3 spends con-
 350 siderable time in the magnetosphere (Figure 11).

351 Here we show neither any correlation calculation nor comparison plot. In the mag-
 352 netosphere, the GUMICS–4 does not work well. Neither the magnetic field nor the plasma
 353 moments nor the N_{EFW} fit well. The solar wind velocity does not reach zero in the sim-
 354 ulation. Instead, the solar wind enters the night side magnetosphere. The solar wind CIS
 355 HIA ion plasma density and the calculated density from spacecraft potential increase closer
 356 to the Earth (plasmasphere). The GUMICS–4 density is low there. We calculated the
 357 dipole field in GSE using Tsyganenko Geotool box [Tsyganenko, 1995] and subtracted
 358 from both the observed and the simulated magnetic field B_z data. The correlation of these
 359 corrected magnetic field measurements and simulations is very low too.

360 **3.4 Bow shock, magnetopause, neutral sheet**

361 77 intervals are selected when [...] Cluster SC3 crossed the terrestrial bow shock
 362 once or multiple times (**Table 6**). When the spacecraft crosses the bow shock **inbound**
 363 the magnitude of the magnetic field and the solar wind density increases **by a factor**
 364 **of 4–5 times** (from 5 nT or 5 cm^{-3} , respectively), the solar wind speed drops from 400–
 365 600 km/s to 100–300 km/s; furthermore the narrow band ~~on~~ the omnidirectional Clus-
 366 ter CIS HIA ion spectra [...] widens. **Both** the Cluster measurements and the GUMICS–4
 367 simulations **have 5-min resolution and are interpolated to 1-min resolution**. All
 368 bow shock transitions of the virtual spacecraft are slower and smoother. Additionally,
 369 ~~the~~ multiple bow shock transitions ~~are not visible in the GUMICS simulations~~. The code
 370 reacts slowly to such sudden changes. The magnetic signatures fit better than the cal-
 371 culated plasma moments. The jump of the ion plasma parameters and the derived Clus-
 372 ter EFW density of the simulations are shifted to the measurements. Generally, the den-

373 sity and the velocity of the simulations seem to be less accurate than the magnetic field
 374 of the simulations.

375 **54** intervals are selected around magnetopause crossings [...] (**Table 7**). When
 376 the spacecraft crosses the magnetopause **inbound** the magnitude of the magnetic field
 377 increases, the solar wind speed drops from 100–300 km/s to zero, the plasma density be-
 378 comes zero; furthermore the wide band on the omnidirectional Cluster CIS HIA ion spec-
 379 tra disappears. [...] The location of the magnetopause is well determined by the Clus-
 380 ter SC3 measurements. However, it is very difficult to identify the magnetopause cross-
 381 ings in the simulation data. [...] The magnetopause crossings very often cannot be seen
 382 in the simulations. Or when the magnetopause crossings are identified in both simula-
 383 tions and spacecraft measurements the events are shifted. The accuracy of the model
 384 is lower for the dayside magnetopause locations.

385 Nine intervals are chosen around Cluster SC3 neutral sheet crossings (Figure 12;
 386 Table 8). The neutral **sheet** locations **are** determined using the results of the Bound-
 387 ary Layer Identification Code (BLIC) Project [Facskó *et al.*, in preparation]. The BLIC
 388 code determines the neutral sheet crossing Cluster FGM magnetic field measurements
 389 using Wang and Xu [1994]’s method. When the solar wind speed is almost zero; further-
 390 more the CIS HIA density and the EFW calculated density are almost zero too; finally
 391 the GSE Z component of the magnetic field changes is a sign of the code indicated neu-
 392 tral sheet crossing (Figure 19; red and blue curves). [...] The neutral sheet crossings
 393 are visible very well in the GUMICS simulations (Figure 19; black curves). For five events
 394 (from nine Cluster SC3 crossings) the GUMICS–4 also provides similar smoothed pa-
 395 rameters and change of sign of the B_z component. This is a **outstanding** result because
 396 the tail in the GUMICS–4 simulations is significantly smaller than the observed real-
 397 ity [Gordeev *et al.*, 2013; Facskó *et al.*, 2016]; furthermore the solar wind enters the tail
 398 in MHD simulations generally [Kallio and Facskó, 2015].

399 4 Discussion

400 The agreement of [...] B_z , V_x and n_{EFW} **in the solar wind** with the similar GU-
 401 MICS simulation **predictions** is very good (Figure 4a, 4b, 4c, blue). The agreement of
 402 [...] n_{CIS} is worse (Figure 4c, red). It was expected because the n_{EFW} depends on the
 403 spacecraft potential provided by the EFW instrument. However, the CIS instrument has

many modes for measuring the plasma parameters and it needs **periodic** calibration too. The correlation of the solar wind V_x , n_{CIS} and n_{EFW} with the similar GUMICS simulation parameters is greater than 0.9 (Figure 5c, 5e, 5g). The correlation of the B_z is also greater than 0.8 (Figure 5a). [...] The **upstream boundary** of the GUMICS–4 code **lies** at $32 R_E$ [Janhunen et al., 2012], the nose of the terrestrial bow shock is at about $20 R_E$. If the solar wind speed is 400 km/s, then this spatial distance means less than a 5 minutes delay, so it should not be visible **in the time delays from the cross correlations**. 80% of the intervals support this theory but 20 % **do** not. In these cases, the one-minute resolution B_z , n_{CIS} or the n_{EFW} parameters have a sudden jump or variation that the simulation cannot follow, or the resolution of the simulation **output** (5 minutes) is too small to see these variations. Therefore, the correlation calculation is not accurate in these cases. Previously the OMNI data was compared to the Cluster data and the Cluster measurements were compared to the GUMICS–4 [Facsikó et al., 2016]. The comparison suggests that the GUMICS–4 results should be similar **for** the OMNI data. Furthermore, we calculate correlation functions in the solar wind, where there is no significant perturbation of the input parameters in the simulation box. Therefore, we get **the** expected result after comparing the two different correlation calculations.

In the magnetosheath we get worse agreement with the GUMICS simulation data (Figure 9a, 9b, 9c). **While the parameters are correlated, the scatter is greater.** The general reason **for** this larger uncertainty seems to be [...] **that the magnetosheath is turbulent.** This phenomenon explains the higher variations of the B_z magnetic field on Figure 9a. The solar wind V_x , n_{CIS} and n_{EFW} agree better than the magnetic field component (Figure 9b, 9c). Here there is no deviation between the densities derived in different ways (n_{CIS} and n_{EFW}) on Figure 9c. Figure 10 seems to contradict these statements above. The larger uncertainty of the B_z is visible in Figure 10a. However, that correlation is still good in Figure 10b. The other parameters have larger (> 0.9) correlation in Figure 10c, 10e, 10g. However, the time shifts in Figure 10d, 10f, 10h seem to be worse. Here the time shifts are worse because the shape of the time series in the magnetosheath looks very **smooth and similar hence there are not enough points to get a sharp and large maximum correlation as the function of timeshift.** **The difference between the minimum and the maximum of the correlation is small comparing with the uncertainty of the calculation.** The maximum, the timeshift could be anywhere and the shape of the correlation vs. timeshift

437 function is often neither symmetric nor has only one local maximum. Hence,
 438 the correlation calculation provides larger time shifts for the ion plasma parameters and
 439 the n_{EFW} .

440 In the magnetosphere the GUMICS–4 does not work well. [...] GUMICS–4 uses
 441 a tilted dipole to describe the terrestrial magnetic field [Janhunen et al., 2012]. After re-
 442 moving the magnetic dipole from the magnetic field measurements of the Cluster SC3
 443 and the simulation we get very low correlations and unacceptable time shifts (not shown).
 444 [...] The tilted dipole is an insufficient description **of the inner magnetospheric mag-**
 445 **netic field.** [...] The plasma **moments** and the n_{EFW} do not fit either. **The single**
 446 **fluid, ideal MHD does not describe the inner magnetosphere well** therefore [...]
 447 V_x and [...] n in the simulations do not agree **with** V_x , [...] n_{CIS} and the n_{EFW} mea-
 448 **sured by the Cluster SC3.** Within the $3.7 R_E$ domain **ring current physics must be**
 449 **added, as it has been** in other global MHD codes [for example Tóth et al., 2012].
 450 This [...] can explain [...] the limited accuracy of the cross polar cap potential (CPCP)
 451 and geomagnetic indices of the GUMICS simulations [Juusola et al., 2014]. The CPCP
 452 [...] GUMICS **agrees well with** spacecraft measurements therefore this quantity could
 453 be used for [...] simulation studies [Lakka et al., 2018a]. Haiducek et al. [2017] also [...]
 454 **compared** [...] geomagnetic indices and the CPCP. The Space Weather Modelling Frame-
 455 work (SWMF) was tested. When the inner magnetosphere model was switched off in the
 456 simulation only the comparison of the simulated and observed CPCP was good. There-
 457 fore, the reason of the discrepancy of the geomagnetic indices in the GUMICS simula-
 458 tions must be the missing inner magnetosphere model.
 ↴

459 The reason ~~of~~ why simulation results and [...] measurements disagree
 460 could be the code or ~~the~~ bad input parameters. During the 1-year run the
 461 distributions of the OMNI solar wind magnetic field B_x , B_y , B_z components
 462 [...] ; solar wind velocity V_x , V_y V_z components [...] and the solar wind P dy-
 463 namic pressure are calculated [...] from January 29, 2002 to February 2, 2003
 464 in GSE reference frame. These distributions of the OMNI solar wind mag-
 465 netic field B_x , B_y , B_z components were overplotted by red in Figure 13a, 13d, 13g, 13j
 466 and Figure 16a, 16d, 16g, 16j; Figure 13b, 13e, 13h, 13k and Figure 16b, 16e, 16h, 16k;
 467 furthermore Figure 13c, 13f, 13i, 13l and Figure 16c, 16f, 16i, 16l. These dis-
 468 tributions of the OMNI solar wind velocity V_x , V_y , V_z components were over-
 469 plotted by red in Figure 14a, 14d, 14g, 14j and Figure 17a, 17d, 17g, 17j; Fig-

ure 14b, 14e, 14h, 14k and Figure 17b, 17e, 17h, 17k; furthermore Figure 14c, 14f, 14i, 14l and Figure 17c, 17f, 17i, 17l. These distributions of the P solar wind pressure calculated from the OMNI solar wind parameters were overplotted by red in Figure 15a, 15b, 15c, 15d and Figure 18a, 18b, 18c, 18d. The intervals when the GUMICS–4 simulations and the Cluster SC3 measurements disagreed are collected for intervals in the solar wind (Table 4) and the magnetosheath (Table 5). The definition of disagreement of the simulations and measurements is quite arbitrary. When the two curves deviate or the correlation function is not symmetric we considered the simulations and the measurements disagreeing. The correlations correlation [coefficients](#) are also high in this cases however the time shift is large (~ 60 min). The averaged shifted OMNI parameters of the poorly agreeing intervals from the Tables 4 and 5 are saved. The distributions of the OMNI parameters belonging to the bad simulation results are calculated for the solar wind region (Figure 13, 14 and 15) and in the magnetosheath (Figure 16, 17 and 18).

1. In the solar wind the distributions of the OMNI B_x , B_y and B_z can be compared in Figure 13a, 13d, 13g, 13j; Figure 13b, 13e, 13h, 13k; furthermore in Figure 13c, 13f, 13i, 13l.
- (a) When the B_z disagrees in simulations and measurements in Figure 13a, 13b, 13c the black and red distributions of the OMNI B_x , B_y and B_z are not similar [...]. The reason of these strange spikes is that there is only one poorly correlated interval for the B_z in the solar wind according to Table 4.
 - (b) When the V_x disagrees in simulations and measurements in Figure 13d, 13e, 13f the black and red distributions of the OMNI B_x , B_y and B_z are similar [...]. The distributions do not agree perfectly because in Table 4 the number of the poorly correlated intervals is only six for the V_x component.
 - (c) When the n_{CIS} disagrees in simulations and measurements in Figure 13g, 13h, 13i the black and red distributions of the OMNI B_x , B_y and B_z are similar [...]. The distributions do not agree perfectly because in Table 4 the number of the poorly correlated intervals is only 12 for the n_{CIS} .

502 (d) When the n_{EFW} disagrees in Figure 13j, 13k, 13l the black and red
 503 distributions of the OMNI B_x , B_y and B_z are similar [...] . The dis-
 504 tributions do not agree perfectly because in Table 4 the number of
 505 the poorly correlated intervals is only nine for n_{EFW} .

506 The values of the OMNI B_x , B_y , and B_z are not peculiar in the solar
 507 wind.

508 2. In the solar wind the distributions of the OMNI V_x , V_y and V_z can be
 509 compared in Figure 14a, 14d, 14g, 14j; Figure 14b, 14e, 14h, 14k; fur-
 510 thermore in Figure 14c, 14f, 14i, 14l.

511 (a) When the B_z disagrees in Figure 14a, 14b, 14c the black and red dis-
 512 tributions of the OMNI V_x , V_y and V_z are not similar [...] . The rea-
 513 son of these strange spikes is that there is only one poorly correlated
 514 interval for the B_z in the solar wind according to Table 4.

515 (b) When the V_x disagrees in simulations and measurements in Figure 14d, 14e, 14f
 516 the black and red distributions of the OMNI V_x , V_y and V_z are sim-
 517 ilar [...] . The distributions do not agree perfectly because in Table 4
 518 the number of the poorly correlated intervals is only six for the V_x
 519 component.

520 (c) When the n_{CIS} disagrees in Figure 14g, 14h, 14i the black and red
 521 distributions of the OMNI V_x , V_y and V_z are similar [...] . The dis-
 522 tributions do not agree perfectly because in Table 4 the number of
 523 the poorly correlated intervals is only 12 for the n_{CIS} .

524 (d) When the n_{EFW} disagrees in simulations and measurements in Fig-
 525 ure 14j, 14k, 14l the black and red distributions of the OMNI V_x , V_y
 526 and V_z are similar [...] . The distributions do not agree perfectly be-
 527 cause in Table 4 the number of the poorly correlated intervals is only
 528 nine for the n_{EFW} .

529 The values of the OMNI V_x , V_y , and V_z are not peculiar in the solar wind.

530 3. In the solar wind the distributions of the solar wind P calculated from
 531 OMNI parameters can be compared in Figure 15a, 15b, 15c, 15d.

532 (a) When the B_z disagrees in Figure 15a the black and red distributions
 533 of the OMNI P are not similar [...] . The reason of these strange spike

- 534 is that there is only one poorly correlated interval for the B_z in the
 535 solar wind according to Table 4.
- 536 (b) When the V_x disagrees in simulations and measurements in Figure 15b
 537 the black and red distributions of the OMNI P are similar [...] . The
 538 distributions do not agree perfectly because in Table 4 the number
 539 of the poorly correlated intervals is only six V_x component.
- 540 (c) When the n_{CIS} disagrees in simulations and measurements in Figure 15c
 541 the black and red distributions of the OMNI P are similar [...] . The
 542 distributions do not agree perfectly because in Table 4 the number
 543 of the poorly correlated intervals is only 12 for the n_{CIS} .
- 544 (d) When the n_{EFW} disagrees in simulations and measurements in Fig-
 545 ure 15d the black and red distributions of the OMNI P are similar
 546 [...] . The distributions do not agree perfectly because in Table 4 the
 547 number of the poorly correlated intervals is only nine for the n_{EFW} .

548 The values of the OMNI P are not peculiar in the solar wind.

549 4. In the magnetosheath the distributions of the OMNI B_x , B_y and B_z can
 550 be compared in Figure 16a, 16d, 16g, 16j; Figure 16b, 16e, 16h, 16k; fur-
 551 thermore in Figure 16c, 16f, 16i, 16l.

- 552 (a) When the B_z disagrees in simulations and measurements in Figure 16a, 16b, 16c
 553 the black and red distributions of the OMNI B_x , B_y and B_z are sim-
 554 ilar [...] .
- 555 (b) When the V_x disagrees in simulations and measurements in Figure 16d, 16e, 16f
 556 the black and red distributions of the OMNI B_x , B_y and B_z are sim-
 557 ilar [...] .
- 558 (c) When the n_{CIS} disagrees in simulations and measurements in Figure 16g, 16h, 16i
 559 the black and red distributions of the OMNI B_x , B_y and B_z are sim-
 560 ilar [...] .
- 561 (d) When the n_{EFW} disagrees in Figure 16j, 16k, 16l the black and red
 562 distributions of the OMNI B_x , B_y and B_z are similar [...] .

563 The distributions agree quite well because in Table 5 the number of the
 564 poorly correlated intervals 18, 50, 33 and 30 for the B_z , the V_x , the n_{CIS}
 565 and n_{CIS} components, respectively. The number of cases is higher and

566 the values of the OMNI B_x , B_y and B_z are not peculiar in the magne-
 567 tosheath.

568 5. In the magnetosheath the distributions of the OMNI V_x , V_y and V_z can
 569 be compared in Figure 17a, 17d, 17g, 17j; Figure 17b, 17e, 17h, 17k; fur-
 570 thermore in Figure 17c, 17f, 17i, 17l.

571 (a) When the B_z disagrees in Figure 17a, 17b, 17c the black and red dis-
 572 tributions of the OMNI V_x , V_y and V_z are similar [...] .

573 (b) When the V_x disagrees in simulations and measurements in Figure 17d, 17e, 17f
 574 the black and red distributions of the OMNI V_x , V_y and V_z are sim-
 575 ilar [...] .

576 (c) When the n_{CIS} disagrees in Figure 17g, 17h, 17i the black and red
 577 distributions of the OMNI V_x , V_y and V_z are similar [...] .

578 (d) When the n_{EFW} disagrees in simulations and measurements in Fig-
 579 ure 17j, 17k, 17l the black and red distributions of the OMNI V_x , V_y
 580 and V_z are similar [...] .

581 The distributions agree quite well because in Table 5 the number of the
 582 poorly correlated intervals 18, 50, 33 and 30 for the B_z , the V_x , the n_{CIS}
 583 and n_{CIS} components, respectively. The number of cases is higher and
 584 the values of the OMNI V_x , V_y and V_z are not peculiar in the magne-
 585 tosheath.

586 6. In the magnetosheath the distributions of the solar wind P calculated
 587 from OMNI parameters can be compared in Figure 18a, 18b, 18c, 18d.

588 (a) When the B_z disagrees in Figure 18a the black and red distributions
 589 of the OMNI P are similar [...] .

590 (b) When the V_x disagrees in simulations and measurements in Figure 18b
 591 the black and red distributions of the OMNI P are similar [...] .

592 (c) When the n_{CIS} disagrees in simulations and measurements in Figure 18c
 593 the black and red distributions of the OMNI P are similar [...] .

594 (d) When the n_{EFW} disagrees in simulations and measurements in Fig-
 595 ure 18d the black and red distributions of the OMNI P are similar
 596 [...] .

597 The distributions agree quite well because in Table 5 the number of the
 598 poorly correlated intervals 18, 50, 33 and 30 for the B_z , the V_x , the n_{CIS}
 599 and n_{CIS} components, respectively. The number of cases is higher and
 600 the values of the OMNI P are not peculiar in the magnetosheath.

601 The inaccuracy of the GUMICS-4 simulations does not depend on the OMNI
 602 parameters in the solar wind and magnetosheath regions. The same study
 603 does not need to be done for the magnetosphere because the deviation of the
 604 measurements and the simulations are so large that it cannot be caused by
 605 the wrong OMNI solar wind parameters.

606 The bow shock positions agree in the GUMICS simulations and the Cluster SC3
 607 measurements. However, the magnetopause locations do not fit well as the bow shock
 608 in simulations and observations. In simulations the location of the magnetopause is de-
 609 termined from peaks in currents density, particle density gradient, or changes in flow
 610 velocity [Siscoe et al., 2001; García and Hughes, 2007; Gordeev et al., 2013, see refer-
 611 ences therein]. In this paper the previously saved simulation parameters along the vir-
 612 tual Cluster SC3 orbit are analysed. The J_y current density component cannot be
 613 calculated from only the Cluster SC3 measurements. Therefore, the above men-
 614 tioned methods cannot be applied. [...] This discrepancy of the magnetopause loca-
 615 tion agrees with the results of Gordeev et al. [2013] and Facskó et al. [2016]. Gordeev et al.
 616 [2013] compared synthetic GUMICS runs with an empirical formula for the magnetopause
 617 locations. Facskó et al. [2016] used OMNI solar wind data as input and got the same re-
 618 sult as Gordeev et al. [2013] and this paper. [...] The neutral sheets are visible in both
 619 simulations and observations (Figure 19, Table 8). This experience is exceptional because
 620 the night side magnetosphere of the GUMICS-4 simulations is small and twisted [Gordeev
 621 et al., 2013; Facskó et al., 2016]. However, in these cases the IMF has no large B_y com-
 622 ponent. From Facskó et al. [2016] we know that the GUMICS has normal long tail (or
 623 night side magnetosphere) if the B_y is small.

624 5 Summary and conclusions

625 Based on the previously created 1-year long GUMICS-4 run global MHD simu-
 626 lation results are compared with Cluster SC3 magnetic field, solar wind velocity and den-
 627 sity measurements along the spacecraft orbit. Intervals are selected when the Cluster SC3

628 and the virtual space probe are situated in the solar wind, magnetosheath and the mag-
 629 netosphere and their correlation are calculated. Bow shock, magnetopause and neutral
 630 sheet crossings are selected and their visibility and relative position are compared. We
 631 achieved the following results:

- 632 1. In the solar wind the correlation coefficient of the B_z , the V_x , the n_{EFW}
 633 and the n_{CIS} are larger than 0.8, 0.9, 0.9 and 0.9, respectively. [...] The
 634 agreement of the B_z , the V_x and the n_{EFW} is very good, furthermore the agree-
 635 ment of the n_{CIS} is also good.
- 636 2. In the magnetosheath the correlation coefficient of the B_z , the V_x , the
 637 n_{EFW} and the n_{CIS} are larger than 0.6, 0.9, 0.9 and 0.9, respectively.
 638 [...] The agreement of the magnetic field component, the ion plasma moments
 639 and the calculated empirical density is a bit worse than in the solar wind. The V_x ,
 640 the n_{EFW} and the n_{CIS} fits better than the B_z component in the magnetosheath.
 641 Their agreement is still good. The reason of the deviation is the turbulent behav-
 642 ior of the slowed down and thermalised turbulent solar wind.
- 643 3. In neither the dayside nor the nightside magnetosphere can the GUMICS–4 pro-
 644 vide realistic results. The simulation outputs and the spacecraft measurement dis-
 645 agree in this region. The reason of this deviation must be the missing coupled in-
 646 ner magnetosphere model. The applied tilted dipole approach is not satisfactory
 647 in the magnetosphere at all.
- 648 4. Disagreement between GUMICS–4 and observations does not seem to
 649 be due to upstream solar wind.
- 650 5. The position of the bow shock and the neutral sheet agrees well in the simulations
 651 and the Cluster SC3 magnetic field, ion plasma moments and derived electron den-
 652 sity measurements in this study. The position of the magnetopause does not fit
 653 that well. [...]

654 The GUMICS–4 has [...] scientific and strategic importance for the European Space
 655 Weather and Scientific community. This code developed in the Finnish Meteorological
 656 Institute is the most developed and tested, widely used tool for modelling the cosmic en-
 657 viroment of the Earth in the Europe. [...] An inner magnetosphere model should
 658 be two way coupled to the existing configuration of the simulation tool to improve the
 659 accuracy of the simulations.

660 **Acknowledgments**

The OMNI data were obtained from the GSFC/SPDF OMNIWeb interface at <http://omniweb.gsfc.nasa.gov>.
 The authors thank the FGM Team (PI: Chris Carr), the CIS Team (PI: Iannis Dandouras),
 the WHISPER Team (PI: Jean-Louis Rauch), the EFW Team (PI: Mats Andre) and the
 Cluster Science Archive for providing FGM magnetic field, CIS HIA ion plasma and WHIS-
 PER electron density measurements. Data analysis was partly done with the QSAS sci-
 ence analysis system provided by the United Kingdom Cluster Science Centre (Impe-
 rial College London and Queen Mary, University of London) supported by the Science
 and Technology Facilities Council (STFC). Eija Tanskanen acknowledges financial sup-
 port from the Academy of Finland for the ReSoLVE Centre of Excellence (project No. 272157).
 Gábor Facskó thanks Anna-Mária Vígh for improving the English of the paper. The au-
 thors thank Pekka Janhunen for developing the GUMICS-4 code; furthermore Minna
 Palmroth and Zoltán Vörös for the useful discussions. The work of Gábor Facskó was
 supported by mission science funding for the Van Allen Probes mission, the American
 Geophysical Union and the HAS Research Centre for Astronomy and Earth Sciences,
 Sopron, Hungary. For further use of the year run data, [...] **request the authors or**
 use the archive of the Community Coordinated Modelling Center (<https://ccmc.gsfc.nasa.gov/publications/posted>)

677

678 **References**

- Balogh, A., M. W. Dunlop, S. W. H. Cowley, D. J. Southwood, J. G. Thomlinson,
 K. H. Glassmeier, G. Musmann, H. Luhr, S. Buchert, M. H. Acuna, D. H. Fair-
 field, J. A. Slavin, W. Riedler, K. Schwingenschuh, and M. G. Kivelson (1997),
 The Cluster Magnetic Field Investigation, *Space Science Reviews*, 79, 65–91, doi:
 10.1023/A:1004970907748.
- Balogh, A., C. M. Carr, M. H. Acuña, M. W. Dunlop, T. J. Beek, P. Brown,
 K. Fornacon, E. Georgescu, K. Glassmeier, J. Harris, G. Musmann, T. Oddy, and
 K. Schwingenschuh (2001), The Cluster Magnetic Field Investigation: overview of
 in-flight performance and initial results, *Annales Geophysicae*, 19, 1207–1217.
- Bartels, J., N. H. Heck, and H. F. Johnston (1939), The three-hour-range index mea-
 suring geomagnetic activity, *Terrestrial Magnetism and Atmospheric Electricity*
(Journal of Geophysical Research), 44, 411, doi:10.1029/TE044i004p00411.
- Blagau, A., I. Dandouras, A. Barthe, S. Brunato, G. Facskó, and V. Constanti-

- 692 nescu (2013), In-flight calibration of Hot Ion Analyser onboard Cluster, *Geo-*
693 *scientific Instrumentation, Methods and Data Systems Discussions*, *3*, 407–435,
694 doi:10.5194/gid-3-407-2013.
- 695 Blagau, A., I. Dandouras, A. Barthe, S. Brunato, G. Facskó, and V. Constantinescu
696 (2014), In-flight calibration of the Hot Ion Analyser on board Cluster, *Geoscientific*
697 *Instrumentation, Methods and Data Systems*, *3*, 49–58, doi:10.5194/gi-3-49-
698 2014.
- 699 Chittenden, J. P., S. V. Lebedev, C. A. Jennings, S. N. Bland , and A. Ciardi
700 (2004), X-ray generation mechanisms in three-dimensional simulations of wire
701 array Z-pinches, *Plasma Physics and Controlled Fusion*, *46*(12B), B457–B476,
702 doi:10.1088/0741-3335/46/12B/039.
- 703 Ciardi, A., S. V. Lebedev, A. Frank, E. G. Blackman, J. P. Chittenden, C. J. Jen-
704 nings, D. J. Ampleford, S. N. Bland, S. C. Bott, J. Rapley, G. N. Hall, F. A.
705 Suzuki-Vidal, A. Marocchino, T. Lery, and C. Stehle (2007), The evolution of
706 magnetic tower jets in the laboratory, *Physics of Plasmas*, *14*(5), 056,501–056,501,
707 doi:10.1063/1.2436479.
- 708 Credland, J., G. Mecke, and J. Ellwood (1997), The Cluster Mission: ESA'S
709 Spacefleet to the Magnetosphere, *Space Science Reviews*, *79*, 33–64, doi:
710 10.1023/A:1004914822769.
- 711 Davis, T. N., and M. Sugiura (1966), Auroral electrojet activity index AE and its
712 universal time variations, *Journal of Geophysical Research*, *71*, 785–801, doi:
713 10.1029/JZ071i003p00785.
- 714 Décréau, P. M. E., P. Fergeau, V. Krasnoselskikh, E. Le Guirriec, M. Lévêque,
715 P. Martin, O. Randriamboarison, J. L. Rauch, F. X. Sené, H. C. Séran, J. G.
716 Trotignon, P. Canu, N. Cornilleau, H. de Féraudy, H. Alleyne, K. Yearby, P. B.
717 Mögensen, G. Gustafsson, M. André, D. C. Gurnett, F. Darrouzet, J. Lemaire,
718 C. C. Harvey, P. Travnicek, and Whisper Experimenters Group (2001), Early re-
719 sults from the Whisper instrument on Cluster: an overview, *Annales Geophysicae*,
720 *19*, 1241–1258, doi:10.5194/angeo-19-1241-2001.
- 721 Escoubet, C. P., M. Fehringer, and M. Goldstein (2001), Introduction The Cluster
722 mission, *Annales Geophysicae*, *19*, 1197–1200, doi:10.5194/angeo-19-1197-2001.
- 723 Facskó, G., I. Honkonen, T. Živković, L. Palin, E. Kallio, K. Ågren, H. Opgenoorth,
724 E. I. Tanskanen, and S. Milan (2016), One year in the Earth's magnetosphere: A

- 725 global MHD simulation and spacecraft measurements, *Space Weather*, 14, 351–
726 367, doi:10.1002/2015SW001355.
- 727 Facskó, G., T. B. Balogh, E. I. Anekallu, C. R. and Tanskanen, P. Peitso, L. Degener,
728 M. Kangwa, T. Laitinen, and S. Laakso, H. Burley (in preparation), Bow shock
729 identification in cluster measurements, *Space Weather*.
- 730 Fazakerley, A. N., A. D. Lahiff, R. J. Wilson, I. Rozum, C. Anekallu, M. West, and
731 H. Bacai (2010a), PEACE Data in the Cluster Active Archive, *Astrophysics and*
732 *Space Science Proceedings*, 11, 129–144, doi:10.1007/978-90-481-3499-1_8.
- 733 Fazakerley, A. N., A. D. Lahiff, I. Rozum, D. Kataria, H. Bacai, C. Anekallu,
734 M. West, and A. Åsnes (2010b), Cluster-PEACE In-flight Calibration Status,
735 *Astrophysics and Space Science Proceedings*, 11, 281–299, doi:10.1007/978-90-481-
736 3499-1_19.
- 737 García, K. S., and W. J. Hughes (2007), Finding the Lyon-Fedder-Mobarry mag-
738 netopause: A statistical perspective, *Journal of Geophysical Research (Space*
739 *Physics)*, 112(A6), A06229, doi:10.1029/2006JA012039.
- 740 Gordeev, E., G. Facskó, V. Sergeev, I. Honkonen, M. Palmroth, P. Janhunen, and
741 S. Milan (2013), Verification of the GUMICS-4 global MHD code using empirical
742 relationships, *Journal of Geophysical Research (Space Physics)*, 118, 3138–3146,
743 doi:10.1002/jgra.50359.
- 744 Greenwald, R. A., K. B. Baker, J. R. Dudeney, M. Pinnock, T. B. Jones, E. C.
745 Thomas, J.-P. Villain, J.-C. Cerisier, C. Senior, C. Hanuise, R. D. Hunsucker,
746 G. Sofko, J. Koehler, E. Nielsen, R. Pellinen, A. D. M. Walker, N. Sato,
747 and H. Yamagishi (1995), Darn/Superdarn: A Global View of the Dynam-
748 ics of High-Latitude Convection, *Space Science Reviews*, 71, 761–796, doi:
749 10.1007/BF00751350.
- 750 Guild, T. B., H. E. Spence, E. L. Kepko, V. Merkin, J. G. Lyon, M. Wiltberger, and
751 C. C. Goodrich (2008a), Geotail and LFM comparisons of plasma sheet clima-
752 tology: 1. Average values, *Journal of Geophysical Research (Space Physics)*, 113,
753 A04216, doi:10.1029/2007JA012611.
- 754 Guild, T. B., H. E. Spence, E. L. Kepko, V. Merkin, J. G. Lyon, M. Wiltberger, and
755 C. C. Goodrich (2008b), Geotail and LFM comparisons of plasma sheet climatol-
756 ogy: 2. Flow variability, *Journal of Geophysical Research (Space Physics)*, 113,
757 A04217, doi:10.1029/2007JA012613.

- 758 Gustafsson, G., R. Bostrom, B. Holback, G. Holmgren, A. Lundgren, K. Stasiewicz,
759 L. Ahlen, F. S. Mozer, D. Pankow, P. Harvey, P. Berg, R. Ulrich, A. Pedersen,
760 R. Schmidt, A. Butler, A. W. C. Fransen, D. Klinge, M. Thomsen, C.-G. Faltham-
761 mar, P.-A. Lindqvist, S. Christenson, J. Holtet, B. Lybekk, T. A. Sten, P. Tan-
762 skanen, K. Lappalainen, and J. Wygant (1997), The Electric Field and Wave
763 Experiment for the Cluster Mission, *Space Science Reviews*, 79, 137–156, doi:
764 10.1023/A:1004975108657.
- 765 Gustafsson, G., M. André, T. Carozzi, A. I. Eriksson, C.-G. Fälthammar, R. Grard,
766 G. Holmgren, J. A. Holtet, N. Ivchenko, T. Karlsson, Y. Khotyaintsev, S. Klimov,
767 H. Laakso, P.-A. Lindqvist, B. Lybekk, G. Marklund, F. Mozer, K. Mursula,
768 A. Pedersen, B. Popielawska, S. Savin, K. Stasiewicz, P. Tanskanen, A. Vaivads,
769 and J.-E. Wahlund (2001), First results of electric field and density observations
770 by Cluster EFW based on initial months of operation, *Annales Geophysicae*, 19,
771 1219–1240, doi:10.5194/angeo-19-1219-2001.
- 772 Haiducek, J. D., D. T. Welling, N. Y. Ganushkina, S. K. Morley, and D. S. Oz-
773 turk (2017), SWMF Global Magnetosphere Simulations of January 2005: Geo-
774 magnetic Indices and Cross-Polar Cap Potential, *Space Weather*, 15, 1567–1587,
775 doi:10.1002/2017SW001695.
- 776 Iyemori, T. (1990), Storm-time magnetospheric currents inferred from mid-latitude
777 geomagnetic field variations, *Journal of Geomagnetism and Geoelectricity*, 42,
778 1249–1265, doi:10.5636/jgg.42.1249.
- 779 Janhunen, P., M. Palmroth, T. Laitinen, I. Honkonen, L. Juusola, G. Facskó, and
780 T. I. Pulkkinen (2012), The GUMICS-4 global MHD magnetosphere-ionosphere
781 coupling simulation, *Journal of Atmospheric and Solar-Terrestrial Physics*, 80,
782 48–59, doi:10.1016/j.jastp.2012.03.006.
- 783 Johnstone, A. D., C. Alsop, S. Burge, P. J. Carter, A. J. Coates, A. J. Coker, A. N.
784 Fazakerley, M. Grande, R. A. Gowen, C. Gurgiolo, B. K. Hancock, B. Narheim,
785 A. Preece, P. H. Sheather, J. D. Winningham, and R. D. Woodliffe (1997), Peace:
786 a Plasma Electron and Current Experiment, *Space Science Reviews*, 79, 351–398,
787 doi:10.1023/A:1004938001388.
- 788 Juusola, L., O. Amm, K. Kauristie, and A. Viljanen (2007), A model for estimating
789 the relation between the Hall to Pedersen conductance ratio and ground magnetic
790 data derived from CHAMP satellite statistics, *Annales Geophysicae*, 25, 721–736,

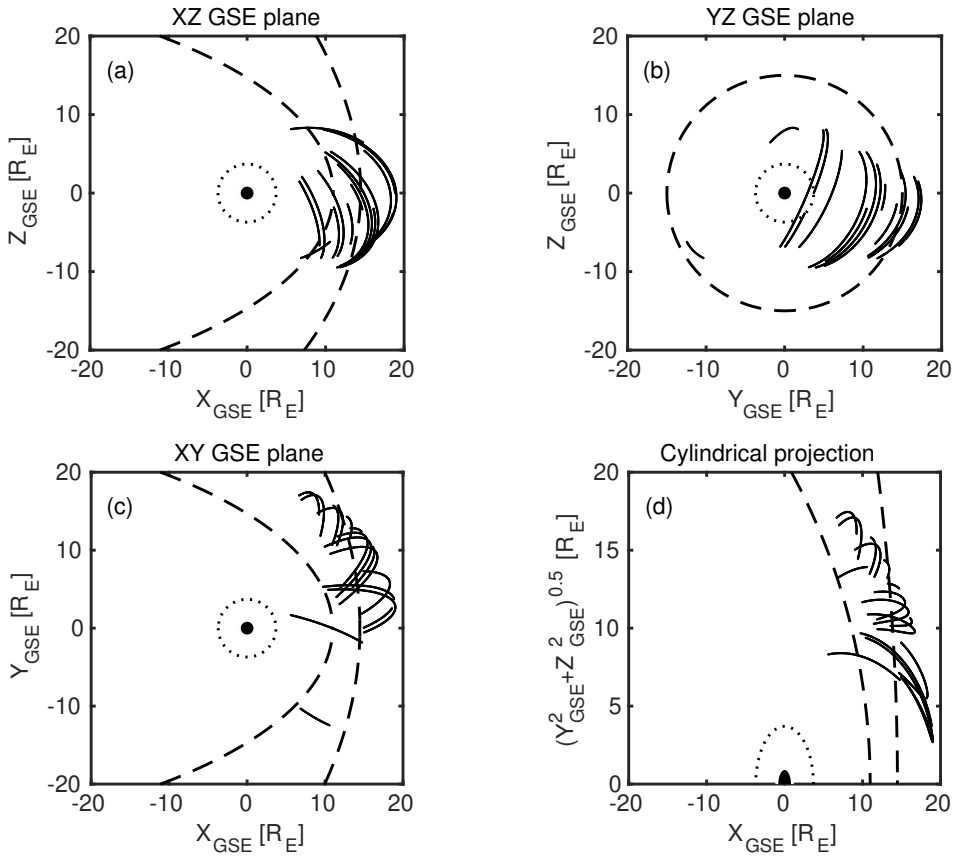
- 791 doi:10.5194/angeo-25-721-2007.
- 792 Juusola, L., G. Facskó, I. Honkonen, P. Janhunen, H. Vanhamäki, K. Kauristie,
 793 T. V. Laitinen, S. E. Milan, M. Palmroth, E. I. Tanskanen, and A. Viljanen
 794 (2014), Statistical comparison of seasonal variations in the GUMICS-4 global
 795 MHD model ionosphere and measurements, *Space Weather*, *12*, 582–600, doi:
 796 10.1002/2014SW001082.
- 797 Kallio, E., and G. Facskó (2015), Properties of plasma near the moon in the magne-
 798 totail, *Planetary and Space Science*, *115*, 69–76, doi:10.1016/j.pss.2014.11.007.
- 799 Kokubun, S., T. Yamamoto, M. H. Acuña, K. Hayashi, K. Shiokawa, and H. Kawano
 800 (1994), The GEOTAIL Magnetic Field Experiment., *Journal of Geomagnetism*
 801 and *Geoelectricity*, *46*, 7–21, doi:10.5636/jgg.46.7.
- 802 Lakka, A., T. I. Pulkkinen, A. P. Dimmock, M. Myllys, I. Honkonen, and M. Palm-
 803 roth (2018a), The Cross-Polar Cap Saturation in GUMICS-4 During High Solar
 804 Wind Driving, *Journal of Geophysical Research (Space Physics)*, *123*, 3320–3332,
 805 doi:10.1002/2017JA025054.
- 806 Lakka, A., T. I. Pulkkinen, A. P. Dimmock, E. Kilpua, M. Ala-Lahti, I. Honko-
 807 nen, M. Palmroth, and Raukunen (2018b), Icme impact at earth with low and
 808 typical mach number plasma characteristics, *Annales Geophysicae Discussions*,
 809 <https://doi.org/10.5194/angeo-2018-81>.
- 810 Lani, A., A. Sanna, N. Villedieu, and M. Panesi (2012), COOLFluiD an Open Com-
 811 putational Platform for Aerothermodynamics and Flow-Radiation Coupling, in
 812 *ESA Special Publication, ESA Special Publication*, vol. 714, p. 45.
- 813 Liemohn, M., N. Y. Ganushkina, D. L. De Zeeuw, L. Rastaetter, M. Kuznetsova,
 814 D. T. Welling, G. Toth, R. Ilie, T. I. Gombosi, and B. van der Holst (2018), Real-
 815 Time SWMF at CCMC: Assessing the Dst Output From Continuous Operational
 816 Simulations, *Space Weather*, *16*(10), 1583–1603, doi:10.1029/2018SW001953.
- 817 Lyon, J. G., J. A. Fedder, and C. M. Mobarry (2004), The Lyon-Fedder-Mobarry
 818 (LFM) global MHD magnetospheric simulation code, *Journal of Atmospheric and*
Solar-Terrestrial Physics, *66*, 1333–1350, doi:10.1016/j.jastp.2004.03.020.
- 819 Mejnertsen, L., J. P. Eastwood, J. P. Chittenden, and A. Masters (2016), Global
 820 MHD simulations of Neptune’s magnetosphere, *Journal of Geophysical Research*
(Space Physics), *121*(8), 7497–7513, doi:10.1002/2015JA022272.
- 821 Mejnertsen, L., J. P. Eastwood, H. Hietala, S. J. Schwartz, and J. P. Chittenden

- 824 (2018), Global MHD Simulations of the Earth's Bow Shock Shape and Motion
825 Under Variable Solar Wind Conditions, *Journal of Geophysical Research (Space*
826 *Physics)*, 123(1), 259–271, doi:10.1002/2017JA024690.
- 827 Mukai, T., S. Machida, Y. Saito, M. Hirahara, T. Terasawa, N. Kaya, T. Obara,
828 M. Ejiri, and A. Nishida (1994), The Low Energy Particle (LEP) Experiment on-
829 board the GEOTAIL Satellite., *Journal of Geomagnetism and Geoelectricity*, 46,
830 669–692, doi:10.5636/jgg.46.669.
- 831 Peredo, M., J. A. Slavin, E. Mazur, and S. A. Curtis (1995), Three-dimensional po-
832 sition and shape of the bow shock and their variation with Alfvénic, sonic and
833 magnetosonic Mach numbers and interplanetary magnetic field orientation, *Jour-*
834 *nal of Geophysical Research*, 100, 7907–7916, doi:10.1029/94JA02545.
- 835 Poedts, S., A. Kochanov, A. Lani, C. Scolini, C. Verbeke, S. Hosteaux, E. Chané,
836 H. Deconinck, N. Mihalache, F. Diet, D. Heynderickx, J. De Keyser, E. De
837 Donder, N. B. Crosby, M. Echim, L. Rodriguez, R. Vansintjan, F. Verstringe,
838 B. Mampaey, R. Horne, S. Glauert, P. Jiggens, R. Keil, A. Glover, G. Deprez, and
839 J.-P. Luntama (2020), The Virtual Space Weather Modelling Centre, *Journal of*
840 *Space Weather and Space Climate*, 10, 14, doi:10.1051/swsc/2020012.
- 841 Powell, K. G., P. L. Roe, T. J. Linde, T. I. Gombosi, and D. L. De Zeeuw (1999), A
842 Solution-Adaptive Upwind Scheme for Ideal Magnetohydrodynamics, *Journal of*
843 *Computational Physics*, 154, 284–309, doi:10.1006/jcph.1999.6299.
- 844 Raeder, J., D. Larson, W. Li, E. L. Kepko, and T. Fuller-Rowell (2008), OpenG-
845 CCM Simulations for the THEMIS Mission, *Space Science Reviews*, 141, 535–555,
846 doi:10.1007/s11214-008-9421-5.
- 847 Reigber, C., H. Lühr, and P. Schwintzer (2002), CHAMP mission status, *Advances*
848 *in Space Research*, 30, 129–134, doi:10.1016/S0273-1177(02)00276-4.
- 849 Reme, H., J. M. Bosqued, J. A. Sauvaud, A. Cros, J. Dandouras, C. Aoustin,
850 J. Bouyssou, T. Camus, J. Cuvilo, C. Martz, J. L. Medale, H. Perrier, D. Rome-
851 fort, J. Rouzaud, C. D'Uston, E. Mobius, K. Crocker, M. Granoff, L. M. Kistler,
852 M. Popecki, D. Hovestadt, B. Klecker, G. Paschmann, M. Scholer, C. W. Carl-
853 son, D. W. Curtis, R. P. Lin, J. P. McFadden, V. Formisano, E. Amata, M. B.
854 Bavassano-Cattaneo, P. Baldetti, G. Bellucci, R. Bruno, G. Chionchio, A. di Lel-
855 lis, E. G. Shelley, A. G. Ghielmetti, W. Lennartsson, A. Korth, H. Rosenbauer,
856 R. Lundin, S. Olsen, G. K. Parks, M. McCarthy, and H. Balsiger (1997), The

- 857 Cluster Ion Spectrometry (CIS) Experiment, *Space Science Reviews*, 79, 303–350,
858 doi:10.1023/A:1004929816409.
- 859 Rème, H., C. Aoustin, J. M. Bosqued, I. Dandouras, B. Lavraud, J. A. Sauvaud,
860 A. Barthe, J. Bouyssou, T. Camus, O. Coeur-Joly, A. Cros, J. Cuvilo, F. Ducay,
861 Y. Garbarowitz, J. L. Medale, E. Penou, H. Perrier, D. Romefort, J. Rouzaud,
862 C. Vallat, D. Alcaydé, C. Jacquey, C. Mazelle, C. D'Uston, E. Möbius, L. M.
863 Kistler, K. Crocker, M. Granoff, C. Mouikis, M. Popecki, M. Vosbury, B. Klecker,
864 D. Hovestadt, H. Kucharek, E. Kuenneth, G. Paschmann, M. Scholer, N. Sckopke,
865 E. Seidenschwang, C. W. Carlson, D. W. Curtis, C. Ingraham, R. P. Lin, J. P.
866 McFadden, G. K. Parks, T. Phan, V. Formisano, E. Amata, M. B. Bavassano-
867 Cattaneo, P. Baldetti, R. Bruno, G. Chionchio, A. di Lellis, M. F. Marcucci,
868 G. Pallocchia, A. Korth, P. W. Daly, B. Graeve, H. Rosenbauer, V. Vasyliunas,
869 M. McCarthy, M. Wilber, L. Eliasson, R. Lundin, S. Olsen, E. G. Shelley, S. Fuse-
870 lier, A. G. Ghielmetti, W. Lennartsson, C. P. Escoubet, H. Balsiger, R. Friedel, J.-
871 B. Cao, R. A. Kovrashkin, I. Papamastorakis, R. Pellat, J. Scudder, and B. Son-
872 nerup (2001), First multispacecraft ion measurements in and near the Earth's
873 magnetosphere with the identical Cluster ion spectrometry (CIS) experiment,
874 *Annales Geophysicae*, 19, 1303–1354, doi:10.5194/angeo-19-1303-2001.
- 875 Ritter, P., H. Lühr, A. Viljanen, O. Amm, A. Pulkkinen, and I. Sillanpää (2004),
876 Ionospheric currents estimated simultaneously from CHAMP satellite and IMAGE
877 ground-based magnetic field measurements: a statistical study at auroral latitudes,
878 *Annales Geophysicae*, 22, 417–430, doi:10.5194/angeo-22-417-2004.
- 879 Rostoker, G. (1972), Geomagnetic indices., *Reviews of Geophysics and Space
880 Physics*, 10, 935–950, doi:10.1029/RG010i004p00935.
- 881 Siscoe, G. L., G. M. Erickson, B. U. Sonnerup, N. C. Maynard, J. A. Schoendorf,
882 K. D. Siebert, D. R. Weimer, W. W. White, and G. R. Wilson (2001), The Mag-
883 netospheric Fluopause, in *AGU Spring Meeting Abstracts*, vol. 2001, pp. SM52D–
884 02.
- 885 Sofko, G. J., R. Greenwald, and W. Bristow (1995), Direct determination of large-
886 scale magnetospheric field-aligned currents with SuperDARN, *Geophysical Re-
887 search Letters*, 22, 2041–2044, doi:10.1029/95GL01317.
- 888 Thomsen, M. F. (2004), Why K_p is such a good measure of magnetospheric convec-
889 tion, *Space Weather*, 2, S11004, doi:10.1029/2004SW000089.

- 890 Tóth, G., I. V. Sokolov, T. I. Gombosi, D. R. Chesney, C. R. Clauer, D. L. de
891 Zeeuw, K. C. Hansen, K. J. Kane, W. B. Manchester, R. C. Oehmke, K. G. Pow-
892 ell, A. J. Ridley, I. I. Roussev, Q. F. Stout, O. Volberg, R. A. Wolf, S. Sazykin,
893 A. Chan, B. Yu, and J. Kóta (2005), Space Weather Modeling Framework: A
894 new tool for the space science community, *Journal of Geophysical Research (Space*
895 *Physics)*, 110, A12226, doi:10.1029/2005JA011126.
- 896 Tóth, G., B. van der Holst, I. V. Sokolov, D. L. De Zeeuw, T. I. Gombosi, F. Fang,
897 W. B. Manchester, X. Meng, D. Najib, K. G. Powell, Q. F. Stout, A. Glo-
898 cer, Y.-J. Ma, and M. Opher (2012), Adaptive numerical algorithms in space
899 weather modeling, *Journal of Computational Physics*, 231, 870–903, doi:
900 10.1016/j.jcp.2011.02.006.
- 901 Trotignon, J. G., P. M. E. Décréau, J. L. Rauch, X. Vallières, A. Rochel,
902 S. Kougblénou, G. Lointier, G. Facskó, P. Canu, F. Darrouzet, and A. Masson
903 (2010), The WHISPER Relaxation Sounder and the CLUSTER Active Archive,
904 *Astrophysics and Space Science Proceedings*, 11, 185–208, doi:10.1007/978-90-481-
905 3499-1_12.
- 906 Trotignon, J.-G., Vallières, and the WHISPER team (2011), Calibration report of
907 the whisper measurements in the cluster active archive (caa), *Tech. rep.*, LPC2E
908 CNRS, caa-est-cr-whi.
- 909 Tsyganenko, N. A. (1995), Modeling the Earth's magnetospheric magnetic field
910 confined within a realistic magnetopause, *Journal of Geophysical Research*, 100,
911 5599–5612, doi:10.1029/94JA03193.
- 912 Vörös, Z., G. Facskó, M. Khodachenko, I. Honkonen, P. Janhunen, and M. Palmroth
913 (2014), Windsock memory COnditioned RAM (CO-RAM) pressure effect: Forced
914 reconnection in the Earth's magnetotail, *Journal of Geophysical Research (Space*
915 *Physics)*, 119, 6273–6293, doi:10.1002/2014JA019857.
- 916 Wang, Z.-D., and R. L. Xu (1994), Signatures of the magnetotail neutral sheet,
917 *Geophysical Research Letters*, 21(19), 2087–2090, doi:10.1029/94GL01960.
- 918 Weimer, D. R. (2005), Improved ionospheric electrodynamic models and applica-
919 tion to calculating Joule heating rates, *Journal of Geophysical Research (Space*
920 *Physics)*, 110, A05306, doi:10.1029/2004JA010884.
- 921 Wiltberger, M., E. J. Rigler, V. Merkin, and J. G. Lyon (2017), Structure of High
922 Latitude Currents in Magnetosphere-Ionosphere Models, *Space Science Reviews*,

- 923 206, 575–598, doi:10.1007/s11214-016-0271-2.
- 924 Zhang, B., W. Lotko, M. J. Wiltberger, O. J. Brambles, and P. A. Damiano (2011),
925 A statistical study of magnetosphere-ionosphere coupling in the Lyon-Fedder-
926 Mobarry global MHD model, *Journal of Atmospheric and Solar-Terrestrial
927 Physics*, 73, 686–702, doi:10.1016/j.jastp.2010.09.027.
- 928 Zhang, B., K. A. Sorathia, J. G. Lyon, V. G. Merkin, J. S. Garretson, and M. Wilt-
929 berger (2019), GAMERA: A Three-dimensional Finite-volume MHD Solver for
930 Non-orthogonal Curvilinear Geometries, *The Astrophysical Journal Supplement
931 Series*, 244(1), 20, doi:10.3847/1538-4365/ab3a4c.



932 **Figure 1.** Cluster SC3 orbit in the solar wind in GSE system for all intervals (see Table 1).
 933 (a) XZ (b) YZ (c) XY (d) Cylindrical projection. Average bow-shock and magnetopause posi-
 934 tions are drawn on all plots using **dashed** lines [Perego *et al.*, 1995; Tsyganenko, 1995, respec-
 935 tively]. The black dots at $3.7 R_E$ show the boundary of the GUMICS-4 inner magnetospheric
 936 domain. The black circle in the origo of all plots shows the size of the Earth.

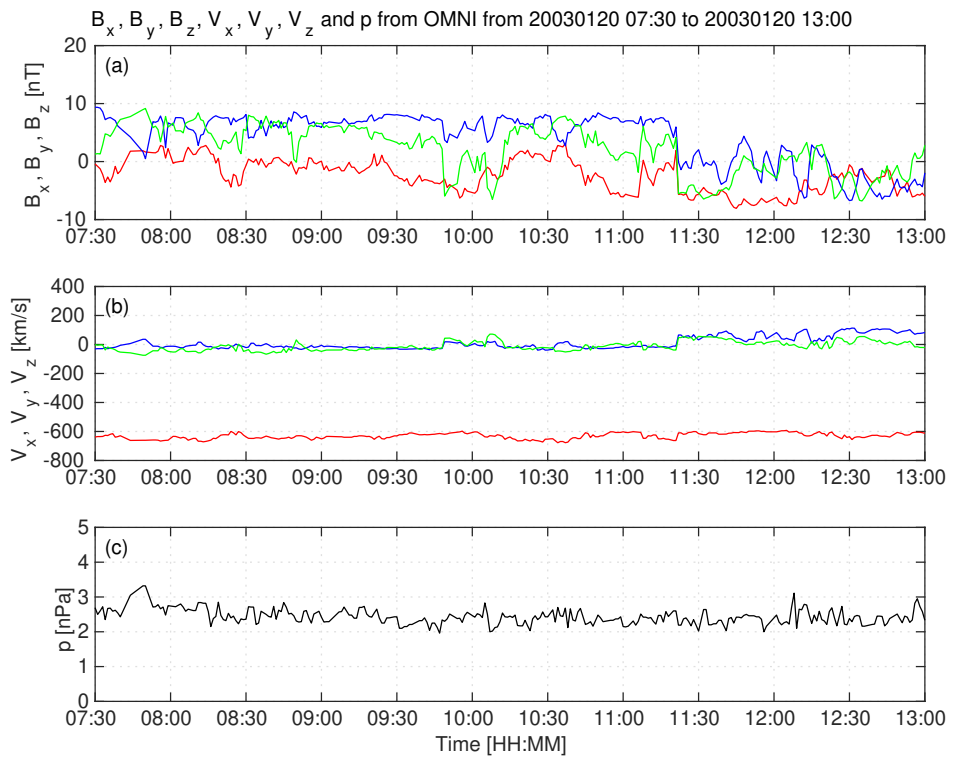
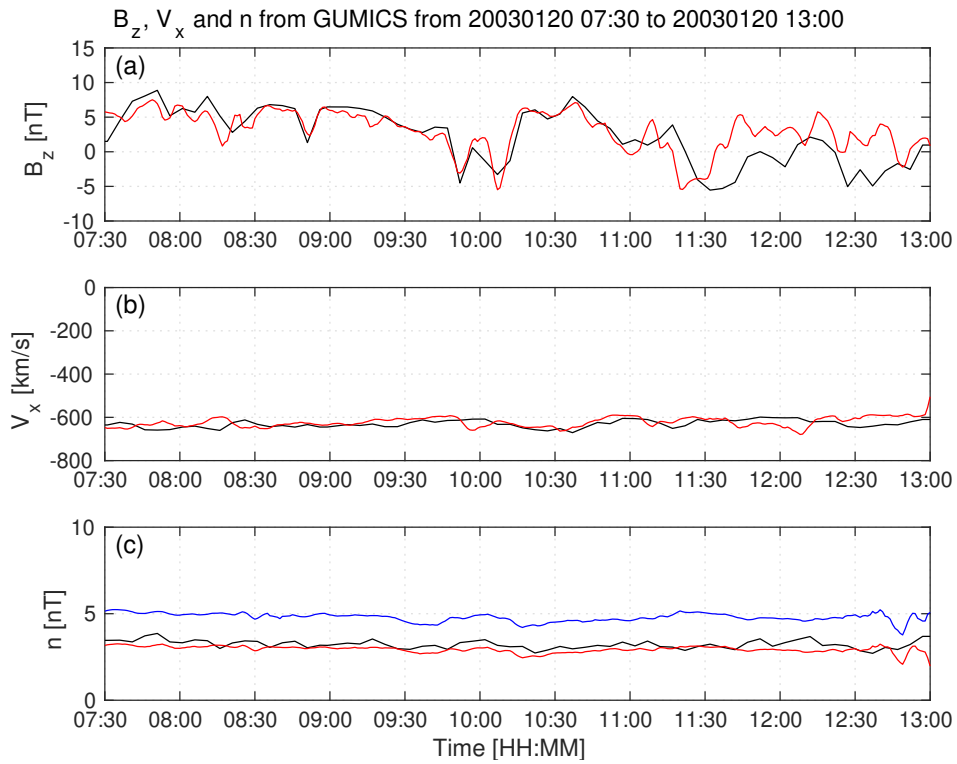


Figure 2. OMNI solar wind data in GSE system from 7:30 to 13:00 (UT) on January 20, 2003. (a) Magnetic field B_x (red), B_y (green) and B_z (blue) components. (b) Solar wind velocity V_x (red), V_y (green) and V_z (blue) components. (c) The P pressure of the solar wind (black).



940 **Figure 3.** GUMICS-4 simulation results (black) and Cluster SC3 magnetic field Z component,
941 ion plasma moments (red) and electron density calculated from spacecraft potential (blue) from
942 January 20, 2003 from 7:30 to 13:00 (UT) in the solar wind in GSE system. (a) Magnetic field Z
943 component. (b) Solar wind velocity X component (c) Solar wind density.

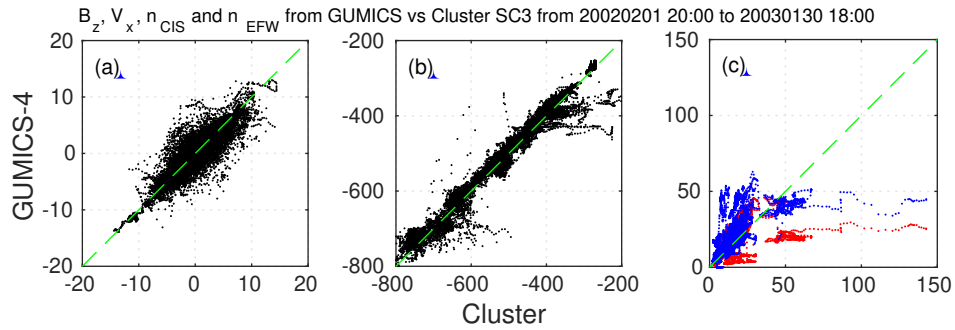
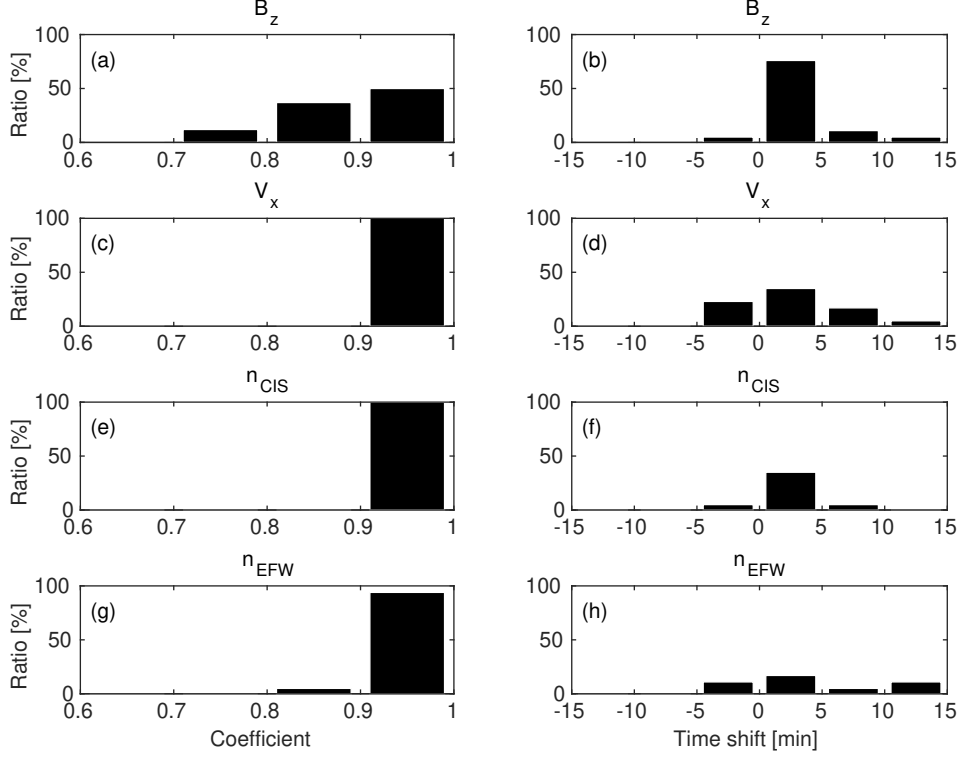
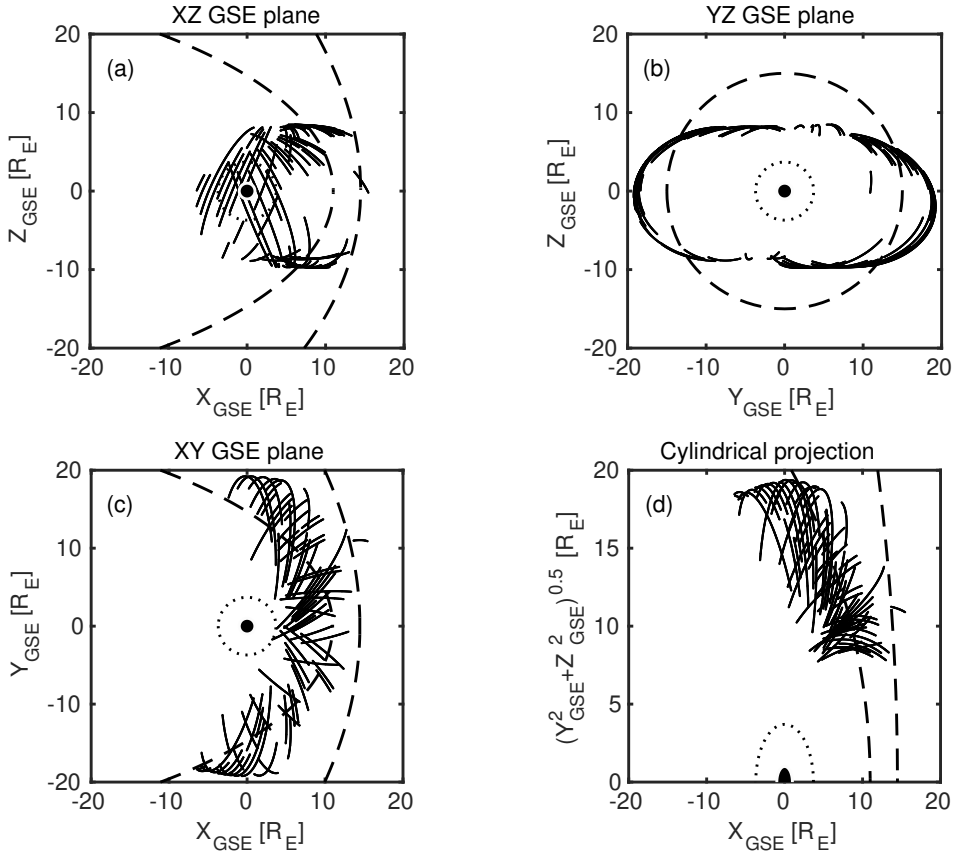


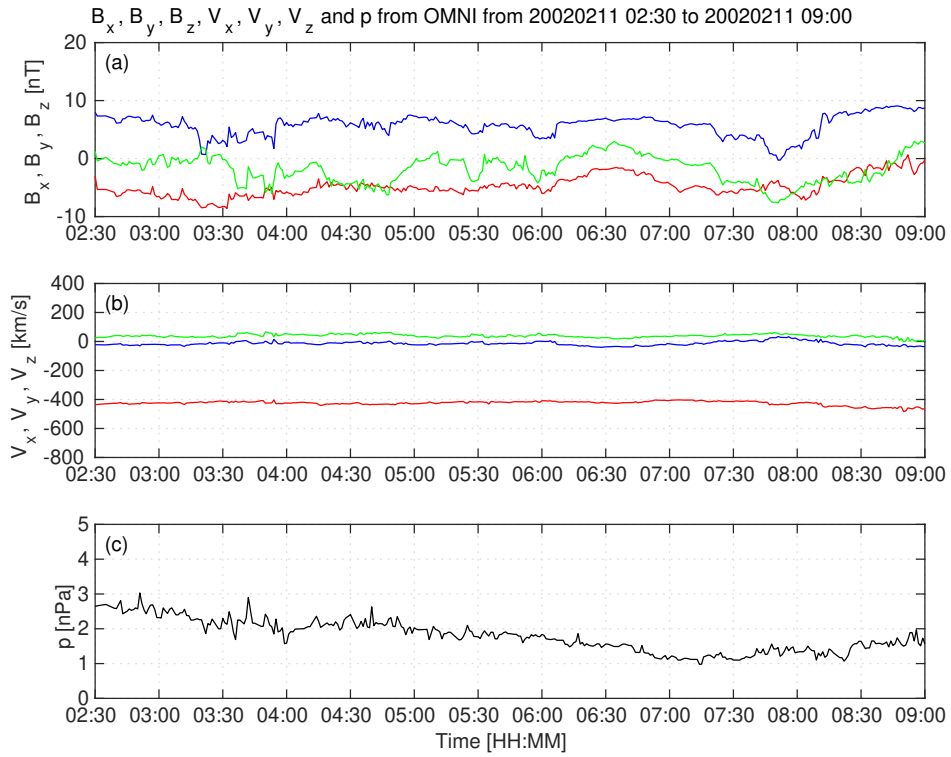
Figure 4. Scattered plots of the Cluster SC3 and GUMICS-4 simulations for all intervals in the solar wind. The dashed line is the $y=x$ line. (a) Magnetic field Z component in GSE system. (b) Solar wind velocity X component in GSE system. (c) Solar wind density measured by the CIS HIA instrument (red) and calculated from the spacecraft potential (blue).



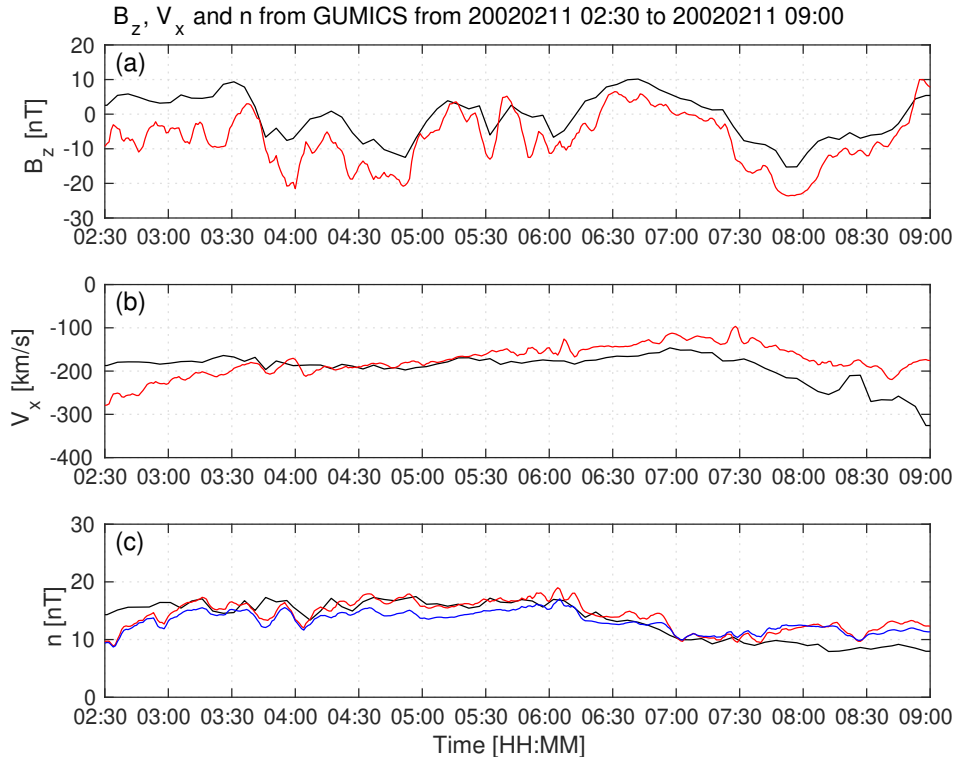
948 **Figure 5.** The distributions of the **highest** correlation coefficients (a, c, e, g) of the magnetic
949 field Z component (B_z) in GSE system, solar wind velocity X component (V_x) in GSE system,
950 the solar wind density measured by the CIS HIA (n_{CIS}) instrument and calculated from the
951 spacecraft potential (n_{EFW}), respectively, for all intervals in the solar wind. The distributions of
952 the **corresponding** time shifts (b, d, f, h) of the B_z , the V_x , the n_{CIS} and the n_{EFW}), respec-
953 tively, for all intervals in the solar wind.



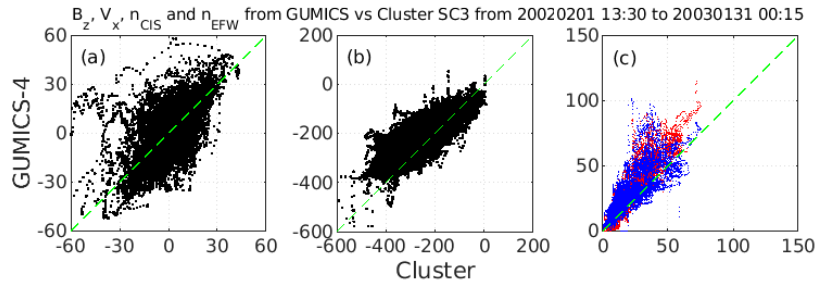
954 **Figure 6.** Cluster SC3 orbit in the magnetosheath in GSE system for all intervals (see Ta-
955 ble 2). (a) XZ (b) YZ (c) XY (d) Cylindrical projection. Average bow-shock and magnetopause
956 positions are drawn on all plots using **dashed** lines [Perez et al., 1995; Tsyganenko, 1995,
957 respectively]. The black dots at $3.7 R_E$ show the boundary of the GUMICS-4 inner magneto-
958 spheric domain. The black circle in the origo of all plots shows the size of the Earth.



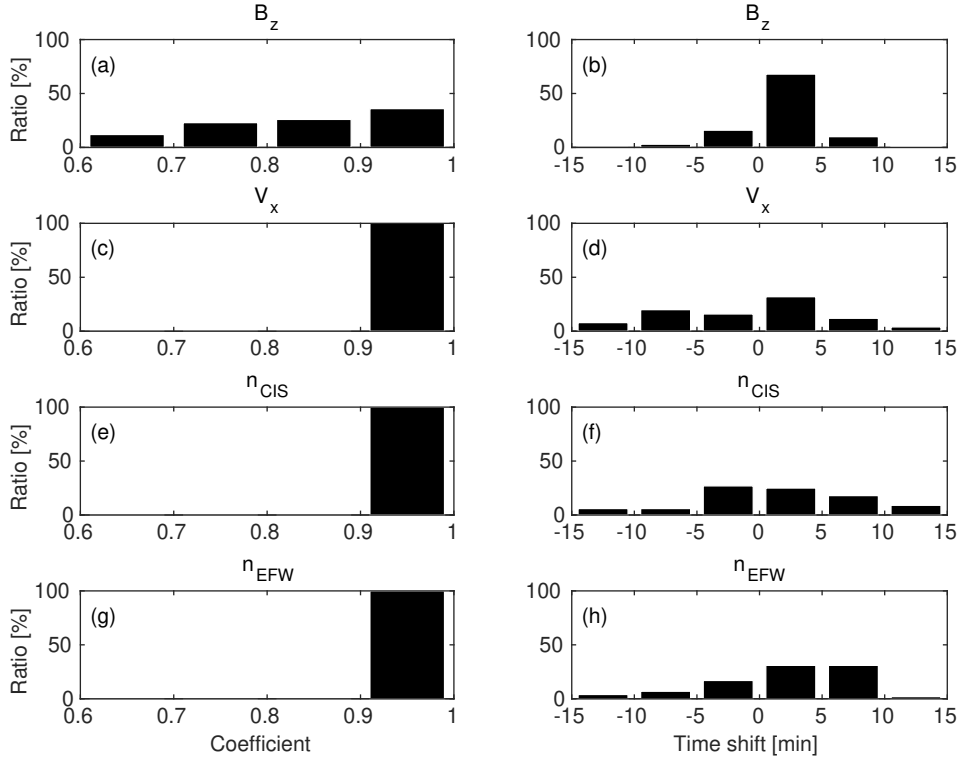
959 **Figure 7.** OMNI solar wind data in GSE system from 2:30 to 09:00 (UT) on February 11,
960 2002. (a) Magnetic field B_x (red), B_y (green) and B_z (blue) components. (b) Solar wind velocity
961 V_x (red), V_y (green) and V_z (blue) components. (c) The P pressure of the solar wind (black).



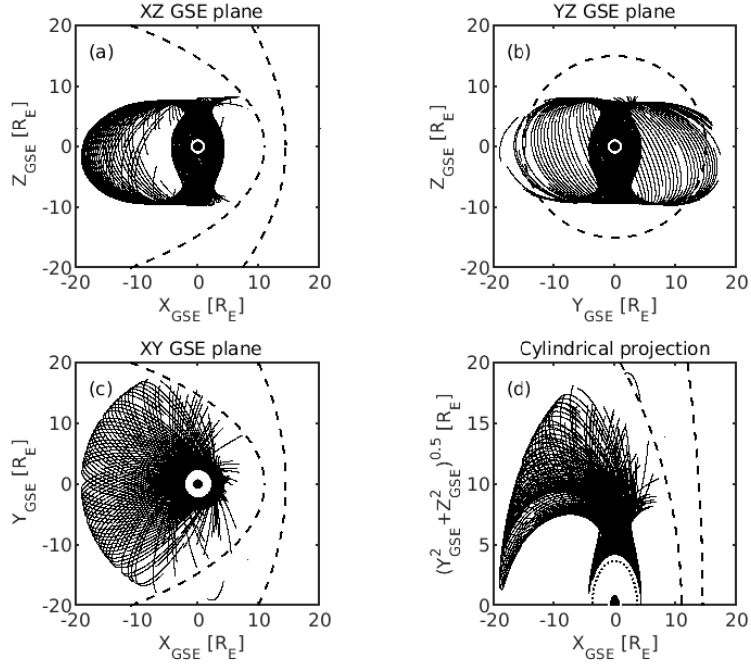
962 **Figure 8.** GUMICS-4 simulation results (black) and Cluster SC3 magnetic field Z component,
963 ion plasma moments (red) and electron density calculated from spacecraft potential (blue) from
964 February 11, 2002 from 2:30 to 9:00 (UT) in the magnetosheath in GSE system (a) Magnetic
965 field Z component. (b) Solar wind velocity X component (c) Solar wind density.



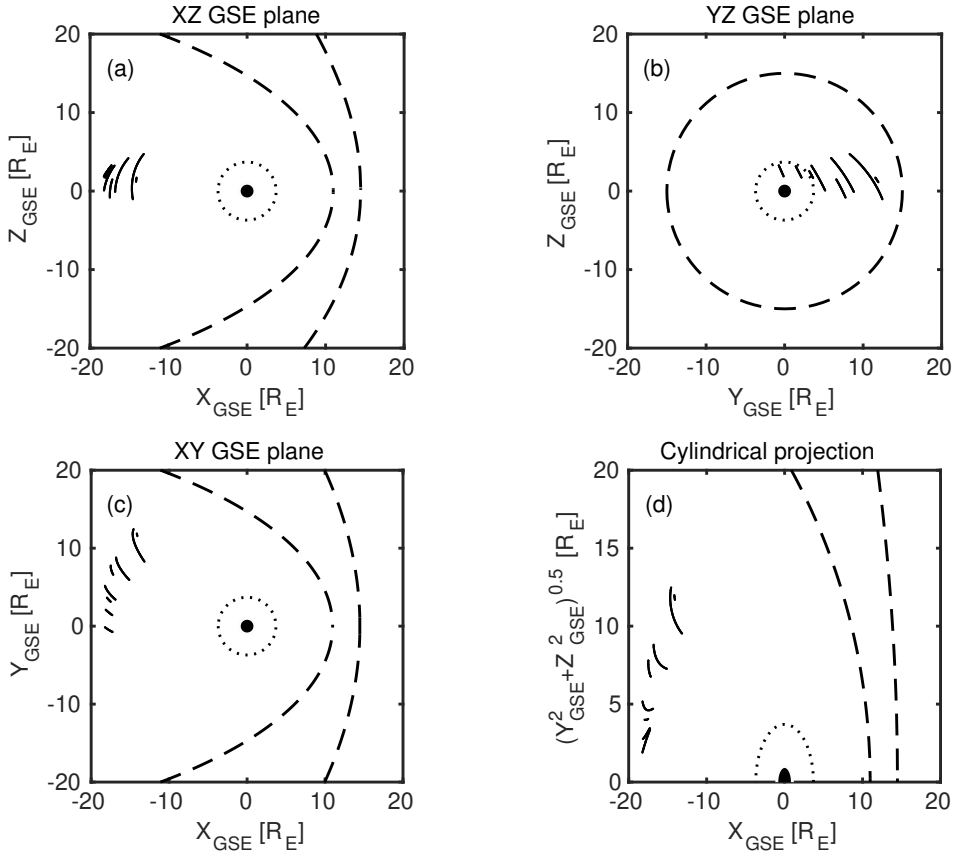
966 **Figure 9.** Scattered plots of the Cluster SC3 and GUMICS–4 simulations for all intervals in
 967 the magnetosheath in GSE system. The dashed line is the $y=x$ line. (a) Magnetic field Z com-
 968 ponent. (b) Solar wind velocity X component. (c) Solar wind density measured by the CIS HIA
 969 instrument (red) and calculated from the spacecraft potential (blue).



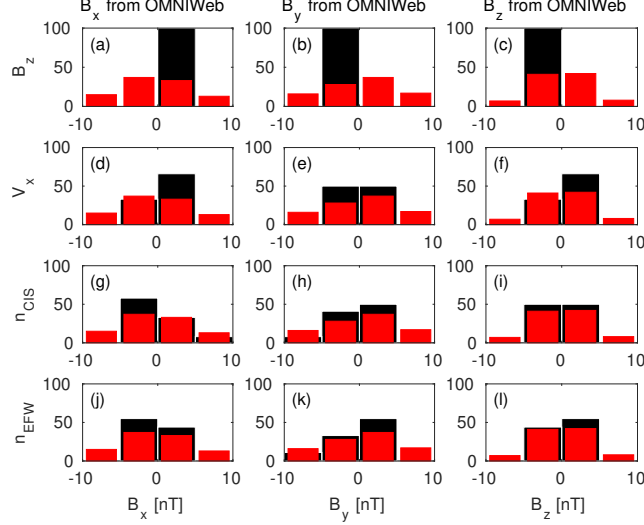
970 **Figure 10.** The distributions of the correlation coefficients (a, c, e, g) of the magnetic field Z
 971 component (B_z) in GSE system, solar wind velocity X component (V_x) in GSE system, the solar
 972 wind density measured by the CIS HIA (n_{CIS}) instrument and calculated from the spacecraft
 973 potential (n_{EFW}), respectively, for all intervals in the magnetosheath. The distributions of the
 974 time shifts (b, d, f, h) of the B_z , the V_x , the n_{CIS} and the n_{EFW} , respectively, for all intervals
 975 in the magnetosheath.



976 **Figure 11.** Cluster SC3 orbit in the magnetosphere in GSE system for all intervals (see Ta-
 977 ble 3). (a) XZ (b) YZ (c) XY (d) Cylindrical projection. Average bow-shock and magnetopause
 978 positions are drawn on all plots using dashed lines [Perez et al., 1995; Tsyganenko, 1995,
 979 respectively]. The black dots at $3.7 R_E$ show the boundary of the GUMICS-4 inner magneto-
 980 spheric domain. The black circle in the origo of all plots shows the size of the Earth.



981 **Figure 12.** Cluster SC3 orbit in the tail in GSE system for all intervals (see Table 8). (a) XZ
 982 (b) YZ (c) XY (d) Cylindrical projection. Average bow-shock and magnetopause positions are
 983 drawn on all plots using **dashed** lines [Perez et al., 1995; Tsyganenko, 1995, respectively]. The
 984 black dots at $3.7 R_E$ show the boundary of the GUMICS–4 inner magnetospheric domain. The
 985 black circle in the origo of all plots shows the size of the Earth.



986 **Figure 13.** The **black** distributions of the B_x , the B_y and the B_z OMNI solar wind magnetic
 987 field components when the agreement of the Cluster SC3 measurements and the GUMICS-4
 988 simulations are poor in the solar wind (see Table 4). The B_z , the V_x , the n_{CIS} and the n_{EFW}
 989 are the magnetic field GSE Z component, the plasma ion velocity X GSE component, the solar
 990 wind density measured by the CIS HIA instrument and the calculated from the EFW spacecraft
 991 potential, respectively. (a, b, c) Distribution of OMNI B_x , B_y , B_z when the agreement of B_z
 992 is poor. (d, e, f) Distribution of OMNI B_x , B_y , B_z when the agreement of V_x is poor. (g, h, i)
 993 Distribution of OMNI B_x , B_y , B_z when the agreement of n_{CIS} is poor. (j, k, l) Distribution of
 994 OMNI B_x , B_y , B_z when the agreement of n_{EFW} is poor. The values are in percentage units in
 995 the distributions. **The red distributions of (a, d, g, j), (b, e, h, k) and (c, f, i, l) are**
 996 **the distribution of the B_x , the B_y , and the B_z components of the OMNI solar wind**
 997 **magnetic field during the 1-year run from January 29, 2002, to February 2, 2003, in**
 998 **GSE reference frame, respectively.**

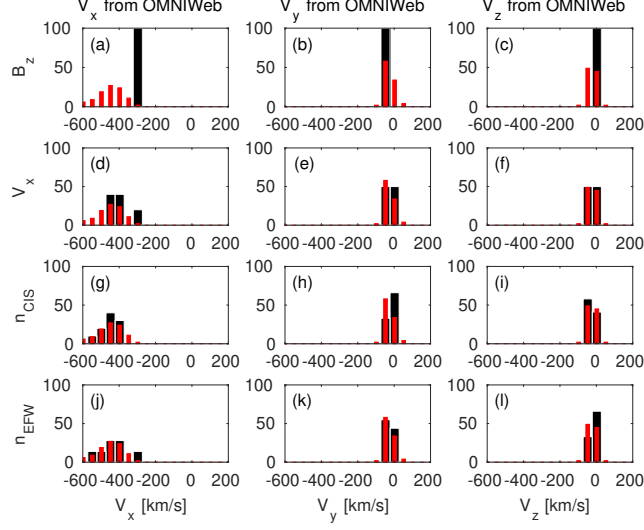
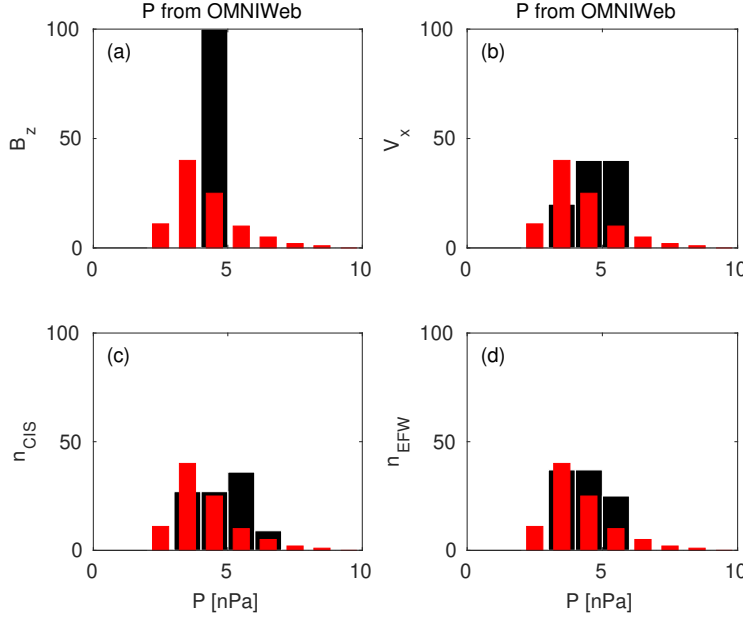
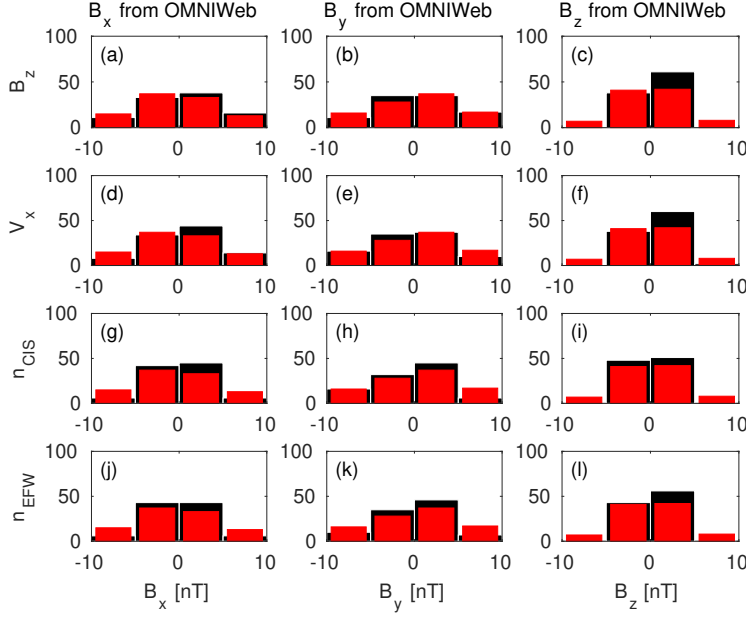


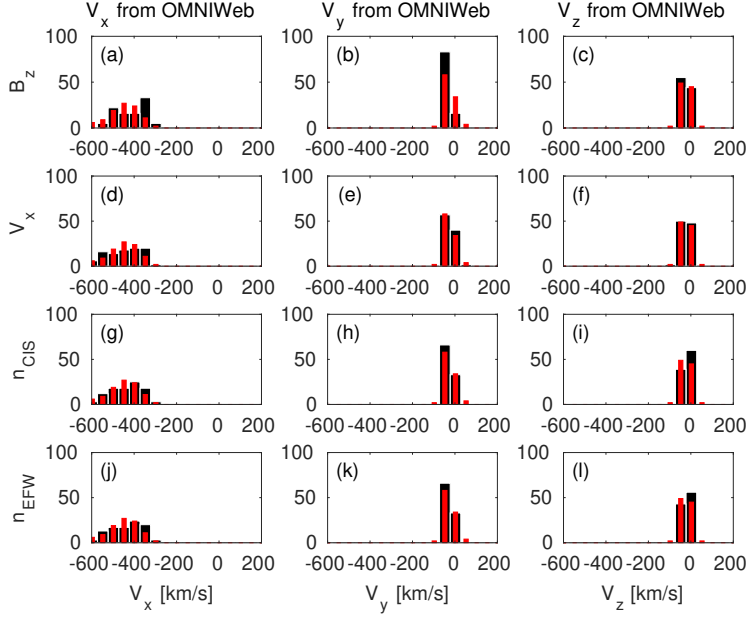
Figure 14. The **black** distributions of the V_x , the V_y and the V_z OMNI solar wind magnetic field components when the agreement of the Cluster SC3 measurements and the GUMICS–4 simulations are poor in the solar wind (see Table 4). The B_z , the V_x , the n_{CIS} and the n_{EFW} are the magnetic field GSE Z component, the plasma ion velocity X GSE component, the solar wind density measured by the CIS HIA instrument and the calculated from the EFW spacecraft potential, respectively. (a, b, c) Distribution of OMNI V_x , V_y , V_z when the agreement of B_z is poor. (d, e, f) Distribution of OMNI V_x , V_y , V_z when the agreement of V_x is poor. (g, h, i) Distribution of OMNI V_x , V_y , V_z when the agreement of n_{CIS} is poor. (j, k, l) Distribution of OMNI V_x , V_y , V_z when the agreement of n_{EFW} is poor. The values are in percentage unit in the distributions. **The red distributions of (a, d, g, j), (b, e, h, k) and (c, f, i, l) are the distributions of the V_x , the V_y and the V_z components of the OMNI solar wind velocity during the 1-year run from January 29, 2002 to February 2, 2003 in GSE reference frame, respectively.**



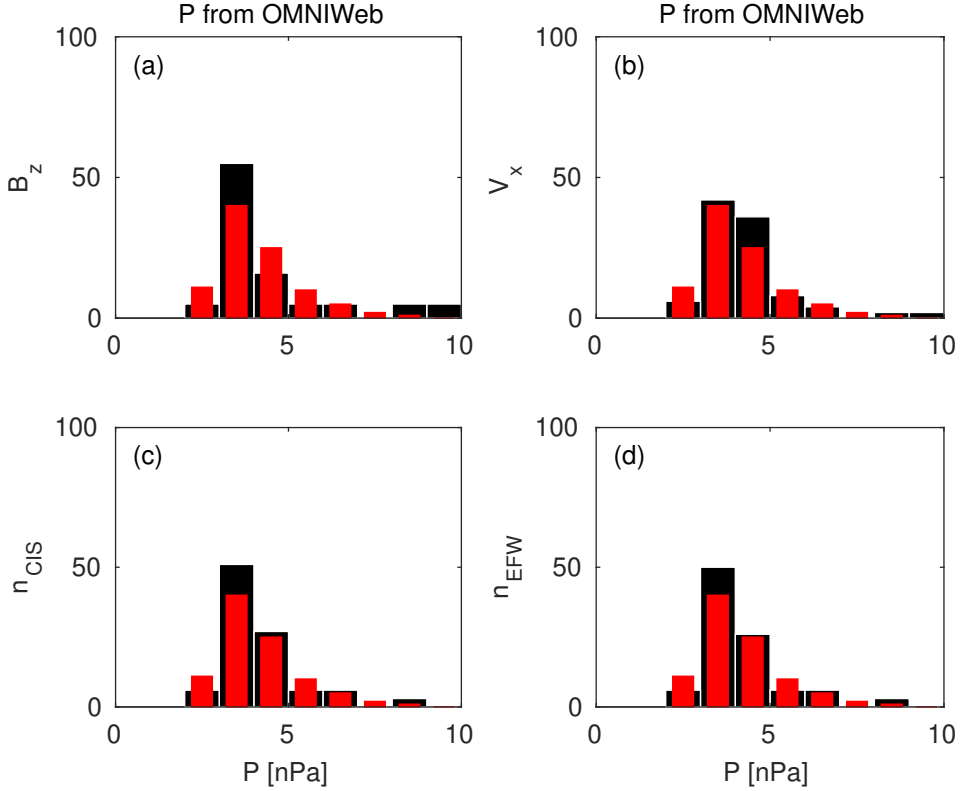
1012 **Figure 15.** The **black** distributions of the P solar wind dynamic pressure calculated from
 1013 OMNI parameters when the agreement of the Cluster SC3 measurements and the GUMICS-4
 1014 simulations are poor in the solar wind (see Table 4). The B_z , V_x , n_{CIS} and n_{EFW} are the mag-
 1015 netic field GSE Z component, the velocity X GSE component, the solar wind density measured
 1016 by the CIS HIA instrument and calculated from the EFW spacecraft potential, respectively.
 1017 (a, b, c, d) The distribution of the P calculated from OMNI data when the agreement of the B_z ,
 1018 the V_x , the n_{CIS} or the n_{EFW} are poor. The values are in percentage unit in the distributions.
 1019 **The red distributions of (a, b, c, d) are the distributions of the P solar wind dy-**
 1020 **namic pressure calculated from the OMNI solar wind parameters during the 1-year**
 1021 **run from January 29, 2002 to February 2, 2003 in GSE reference frame.**



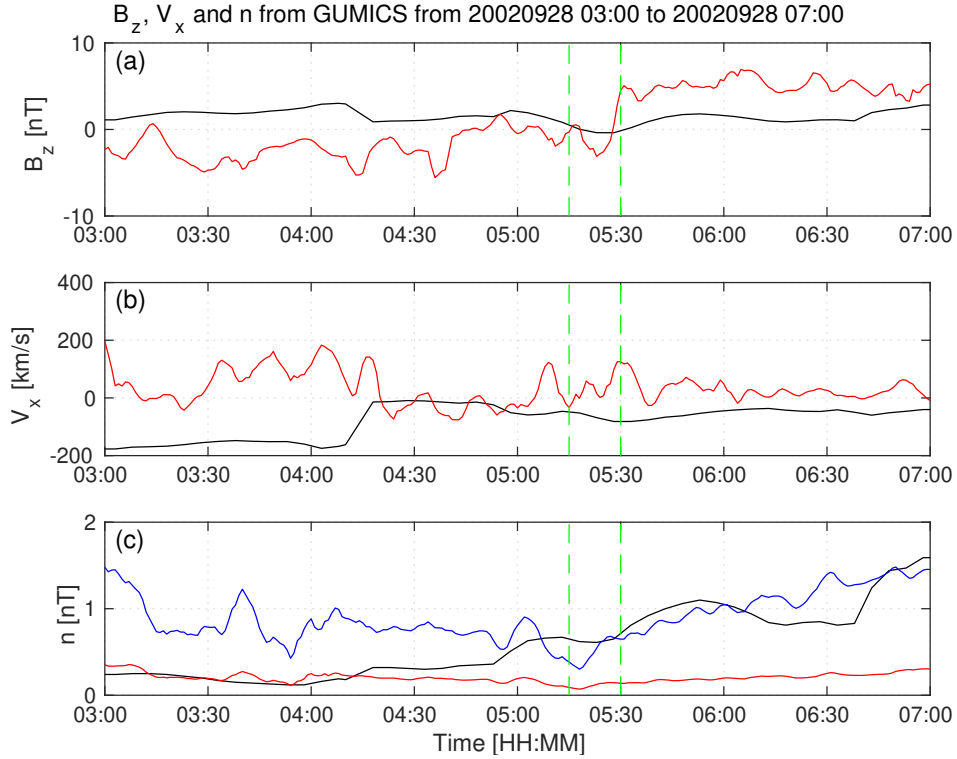
1022 **Figure 16.** The **black** distributions of the B_x , the B_y and the B_z OMNI solar wind magnetic
 1023 field components when the agreement of the Cluster SC3 measurements and the GUMICS–4
 1024 simulations are poor in the magnetosheath (see Table 5). The B_z , the V_x , the n_{CIS} and the
 1025 n_{EWF} are the magnetic field GSE Z component, the plasma ion velocity X GSE component,
 1026 the solar wind density measured by the CIS HIA instrument and the calculated from the EFW
 1027 spacecraft potential, respectively. (a, b, c) Distribution of OMNI B_x , B_y , B_z when the agree-
 1028 ment of B_z is poor. (d, e, f) Distribution of OMNI B_x , B_y , B_z when the agreement of V_x is poor.
 1029 (g, h, i) Distribution of OMNI B_x , B_y , B_z when the agreement of n_{CIS} is poor. (j, k, l) Distri-
 1030 bution of OMNI B_x , B_y , B_z when the agreement of n_{EWF} is poor. The values are in percentage
 1031 unit in the distributions. **The red distributions of (a, d, g, j), (b, e, h, k) and (c, f, i, l)**
 1032 **are the distribution of the B_x , the B_y , and the B_z components of the OMNI solar**
 1033 **wind magnetic field during the 1-year run from January 29, 2002 to February 2,**
 1034 **2003 in GSE reference frame, respectively.**



1035 **Figure 17.** The **black** distributions of the V_x , the V_y and the V_z OMNI solar wind magnetic
 1036 field components when the agreement of the Cluster SC3 measurements and the GUMICS–4
 1037 simulations are poor in the magnetosheath (see Table 5). The B_z , the V_x , the n_{CIS} and the
 1038 n_{EFW} are the magnetic field GSE Z component, the plasma ion velocity X GSE component, the
 1039 solar wind density measured by the CIS HIA instrument and the calculated from the EFW space-
 1040 craft potential, respectively. (a, b, c) Distribution of OMNI V_x , V_y , V_z when the agreement of
 1041 B_z is poor. (d, e, f) Distribution of OMNI V_x , V_y , V_z when the agreement of V_x is poor. (g, h, i)
 1042 Distribution of OMNI V_x , V_y , V_z when the agreement of n_{CIS} is poor. (j, k, l) Distribution of
 1043 OMNI V_x , V_y , V_z when the agreement of n_{EFW} is poor. The values are in percentage unit in
 1044 the distributions. **The red distributions of (a, d, g, j), (b, e, h, k) and (c, f, i, l) are**
 1045 **the distributions of the V_x , the V_y and the V_z components of the OMNI solar wind**
 1046 **velocity during the 1-year run from January 29, 2002 to February 2, 2003 in GSE**
 1047 **reference frame, respectively.**



1048 **Figure 18.** The black distributions of the P solar wind dynamic pressure calculated from
 1049 OMNI parameters when the agreement of the Cluster SC3 measurements and the GUMICS–4
 1050 simulations are poor in the magnetosheath (see Table 5). The B_z , V_x , n_{CIS} and n_{EFW} are
 1051 the magnetic field GSE Z component, the velocity X GSE component, the solar wind density
 1052 measured by the CIS HIA instrument and calculated from the EFW spacecraft potential, respec-
 1053 tively. (a, b, c, d) The distribution of the P calculated from OMNI data when the agreement of
 1054 the B_z , the V_x , the n_{CIS} or the n_{EFW} are poor. The values are in percentage unit in the dis-
 1055 tributions. **The red distributions of (a, b, c, d) are the distributions of the P solar**
 1056 **wind dynamic pressure calculated from the OMNI solar wind parameters during the**
 1057 **1-year run from January 29, 2002 to February 2, 2003 in GSE reference frame.**



1058 **Figure 19.** GUMICS-4 simulation results (black) and Cluster SC3 magnetic field Z compo-
 1059 nent, ion plasma moments (red) and electron density calculated from spacecraft potential (blue)
 1060 from September 28, 2002 from 3:00 to 7:00 (UT) in the tail in GSE system. (a) Magnetic field
 1061 Z component. (b) Solar wind velocity X component (c) Solar wind density. From 05:15 to 05:30
 1062 **between the green dashed vertical lines** both the Cluster SC3 and the virtual spaceprobe of
 1063 the GUMICS-4 simulation cross the neutral sheet multiple times.

Start/End	C_{B_z}	δt_{B_z}	C_{V_x}	δt_{V_x}	$C_{n_{CIS}}$	$\delta t_{n_{CIS}}$	$C_{n_{EFW}}$	$\delta t_{n_{EFW}}$
		[min]		[min]		[min]		[min]
20020201 20:00/0203 04:00	0.97	3	1.00	12	0.96	3	0.98	3
20020211 13:00/0212 12:00	0.86	2	1.00	0	0.99	19	0.99	18
20020218 09:00/0219 02:00	0.95	1	1.00	-4	1.00	-3	0.97	-2
20020219 06:30/0219 15:00	0.96	1	0.99	-1	0.99	-60	1.00	60
20020220 18:30/0222 00:00	0.90	4	1.00	4	0.93	-20	0.98	3
20020318 17:30/0319 02:30	0.91	2	1.00	21	0.98	51	0.99	6
20020412 20:30/0413 02:00	0.91	5	0.99	-53	0.94	60	0.98	12
20021227 12:00/1228 03:00	0.84	4	1.00	-2	0.99	-21	0.99	22
20021229 20:00/1230 16:00	0.76	1	1.00	1	0.99	-30	0.98	43
20030106 06:00/0106 19:00	0.82	5	1.00	7	0.99	3	0.95	-60
20030108 07:00/0109 03:30	0.56	10	1.00	41	0.99	9	0.97	-56
20030113 08:30/0113 18:00	0.94	3	1.00	5	1.00	3	0.97	-1
20030120 07:30/0120 13:00	0.86	3	1.00	8	1.00	4	1.00	-55
20030122 12:00/0123 14:00	0.85	2	1.00	3	1.00	3	0.92	-60
20030124 18:00/0126 00:00	0.78	3	1.00	0	0.99	-60	0.99	60
20030127 16:00/0128 06:00	0.89	-1	1.00	-3	0.96	1	0.89	12
20030129 12:00/0130 18:00	0.92	2	1.00	4	0.95	-59	0.98	1

1064 **Table 1.** The studied solar wind intervals. The correlation coefficients (C_{B_z} , C_{V_x} , $C_{n_{CIS}}$,
1065 $C_{n_{EFW}}$) and time shift (δt_{V_x} , $\delta t_{n_{CIS}}$, $\delta t_{n_{EFW}}$) in minutes of the magnetic field GSE Z compo-
1066 nent (B_z), solar wind velocity X component (V_x), CIS and EFW densities (n_{CIS} , n_{EFW}).

Table 2: The studied magnetosheath intervals. The correlation coefficients (C_{B_z} , C_{V_x} , $C_{n_{CIS}}$, $C_{n_{EFW}}$) and time shift (δt_{V_x} , $\delta t_{n_{CIS}}$, $\delta t_{n_{EFW}}$) in minutes of the magnetic field GSE Z component (B_z), solar wind velocity X component (V_x), CIS and EFW densities (n_{CIS} , n_{EFW}). In the empty slots the correlation calculation gives invalid result.

Start/End	C_{B_z}	δt_{B_z}	C_{V_x}	δt_{V_x}	$C_{n_{CIS}}$	$\delta t_{n_{CIS}}$	$C_{n_{EFW}}$	$\delta t_{n_{EFW}}$
		[min]		[min]		[min]		[min]
20020201 13:30/0201 18:30	0.92	1	0.98	57	0.99	60	0.98	60
20020208 18:15/0209 00:00	0.78	3	0.95	60	0.98	-53	0.98	-54
20020211 02:30/0211 09:00	0.81	0	0.99	-21	1.00	0	0.99	0
20020212 16:30/0212 21:00	0.86	3	1.00	54	0.99	30	0.99	30
20020219 17:30/0219 23:00	0.78	4	0.99	37	1.00	6	1.00	6
20020222 23:00/0223 06:30	0.69	1	0.97	-60	0.99	-52	0.99	-48
20020227 16:30/0227 23:15	0.53	60	0.98	-31	1.00	-38	1.00	-11
20020310 18:30/0311 00:30	0.98	3	0.98	20	0.99	8	0.99	-2
20020311 14:00/0311 19:00	0.88	5	0.97	36	0.99	-3	0.99	-40
20020406 19:00/0407 01:15	0.79	1	0.97	-60	0.98	-56	0.98	-56
20020410 17:30/0410 23:00	0.89	5	0.99	-52	1.00	3	1.00	5
20020411 11:30/0411 16:30	0.84	3	0.99	40	0.99	3	0.99	3
20020418 18:30/0418 22:45	0.93	59	0.99	-60	0.99	60	0.98	60
20020421 04:30/0421 07:45	0.98	55	1.00	-60	1.00	-60	1.00	-60
20020422 11:45/0422 15:45	0.77	-5	0.98	-17	0.99	-15	0.99	-16
20020423 08:30/0423 12:30	0.94	31	1.00	4	0.99	16	1.00	16
20020430 12:30/0430 17:00	0.81	58	0.99	23	0.99	-18		
20020505 07:00/0505 11:15	0.83	59	0.99	32	0.99	-60		
20020506 19:15/0507 00:15	0.89	-28	0.99	-60	0.98	-36		
20020507 17:30/0507 23:00	0.94	1	0.99	47	0.99	-47		
20020514 22:45/0515 03:00	0.82	49	0.99	-60	0.99	32	0.99	-37
20020517 07:00/0517 12:15	0.76	-6	1.00	-5	0.99	-4	0.99	-3
20020518 13:30/0518 19:30	0.76	1	0.99	11	0.98	-2	0.98	-2

Continued on next page

Table 2 – *Continued from previous page*

Start/End	C_{B_z}	δt_{B_z}	C_{V_x}	δt_{V_x}	$C_{n_{CIS}}$	$\delta t_{n_{CIS}}$	$C_{n_{EFW}}$	$\delta t_{n_{EFW}}$
		[min]		[min]		[min]		[min]
20020519 20:00/0520 03:30	0.98	2	1.00	-9	0.99	-4	0.99	-50
20020520 10:45/0520 20:15	0.80	1	0.99	-3	0.95	-1	0.99	-1
20020522 02:00/0522 08:45	0.53	52	0.99	4	0.99	11	0.99	22
20020527 02:15/0527 17:15	0.80	-3	0.99	-2	0.98	0	0.99	0
20020530 05:00/0530 10:30	0.30	3	1.00	-23	0.99	4	0.99	3
20020601 19:30/0602 01:00	0.68	-2	1.00	17	0.99	-6	0.99	-7
20020602 21:45/0603 17:45	0.65	-5	0.99	0	0.98	3	0.99	3
20020605 10:30/0606 06:00	0.20	0	0.99	-7	0.98	10	0.98	9
20020607 18:00/0607 22:00	0.93	-35	1.00	-34	0.99	16	0.99	15
20020608 01:15/0608 18:15	0.54	-4	1.00	-39	0.97	-6	0.97	-6
20020610 01:30/0610 09:30	0.80	5	1.00	8	0.99	3	1.00	-7
20020610 11:00/0611 01:00	0.89	-4	1.00	-35	0.99	24	0.99	7
20020612 18:30/0613 06:15	0.45	-2	0.99	-7	0.97	-3	0.97	-33
20020615 07:00/0615 23:30			1.00	47	0.98	-3	0.98	-5
20020617 05:00/0618 03:45	0.79	3	1.00	28	0.98	9	0.99	8
20020620 04:00/0620 11:00	0.65	-8	0.99	-6	0.98	11	0.98	6
20020622 14:30/0622 18:00	0.99	56	1.00	33	1.00	16	1.00	16
20021201 04:15/1202 07:45	0.41	1	1.00	2	0.99	6	0.99	6
20021203 15:30/1204 19:30	0.72	1	0.99	60	0.98	59	0.98	59
20021207 00:30/1207 07:45	0.53	38	0.99	-50	0.99	-20	0.99	20
20021208 09:30/1209 08:00	0.72	3	0.99	-36	0.98	5	0.98	5
20021212 23:30/1213 14:30	0.53	5	1.00	36	0.99	-3	0.95	-56
20021213 21:15/1214 09:30	0.96	5	1.00	-35	0.99	-5	0.99	-46
20021215 12:45/1216 18:00	0.80	2	0.99	-60	0.95	-60	0.98	30
20021217 16:30/1218 01:45	0.91	2	1.00	-54	0.99	3	0.99	3
20021220 01:30/1220 06:15	0.93	0	1.00	60	0.99	2	0.99	3
20021223 02:15/1223 13:00	0.93	1	0.97	39	0.94	50	0.99	-14
20021223 14:00/1223 22:30	0.88	1	1.00	-2	0.99	-1	1.00	-3
20021224 19:00/1225 01:45	0.96	0	1.00	-43	0.99	12	0.99	28

Continued on next page

Table 2 – *Continued from previous page*

Start/End	C_{B_z}	δt_{B_z}	C_{V_x}	δt_{V_x}	$C_{n_{CIS}}$	$\delta t_{n_{CIS}}$	$C_{n_{EFW}}$	$\delta t_{n_{EFW}}$
		[min]		[min]		[min]		[min]
20021225 23:45/1226 07:15	0.97	7	1.00	-18	0.99	56	0.99	56
20021226 23:00/1227 09:45	0.83	2	1.00	2	0.99	4	0.99	2
20021229 11:45/1229 17:00	0.63	2	1.00	-32	0.99	49	0.99	48
20021230 17:45/1231 01:00	0.74	1	0.99	55	0.98	60	0.98	22
20021231 23:00/0101 05:15	0.92	2	1.00	0	0.99	-54	1.00	-56
20030105 14:00/0105 21:00	0.73	1	1.00	1	1.00	-60	0.99	-60
20030106 23:15/0107 03:00	0.70	4	0.99	41	1.00	56	1.00	-60
20030109 08:45/0109 16:15			0.91	-55	0.98	-13	0.98	-25
20030110 07:15/0110 15:15	0.95	1	0.99	-7	0.99	2	0.98	11
20030111 08:15/0111 22:30	0.88	1	0.99	-59	0.94	-15	0.94	8
20030112 17:30/0113 00:15	0.98	0	1.00	-47	0.99	39	0.99	51
20030114 00:30/0114 08:30	0.86	-1	0.99	-60	0.98	23	0.98	8
20030116 10:15/0116 17:45	0.64	60	0.93	52	0.99	60	0.99	30
20030117 09:30/0117 13:30	0.70	-3	1.00	7	1.00	-31	1.00	-33
20030118 23:30/0119 03:45	0.97	3	1.00	-12	1.00	7	0.99	7
20030119 21:00/0120 01:00	0.96	3	1.00	6	1.00	38	1.00	20
20030121 06:30/0121 11:30	0.87	-3	0.98	40	0.99	8	1.00	8
20030122 04:45/0122 09:30	0.76	-2	1.00	1	1.00	-7	1.00	-4
20030126 01:45/0126 06:30	0.90	3	0.99	-15	1.00	-51	0.99	24
20030127 08:15/0127 13:00	1.00	10	1.00	-60	0.99	-1	0.99	1
20030128 12:30/0128 17:15	0.77	60	0.99	-22	0.99	-5	0.99	21
20030130 19:45/0131 00:15	0.98	2	0.99	52	0.99	8	0.99	8

Table 3: The studied magnetosphere intervals (UT).

Start/End
20020213 23:00/0214 01:30
20020217 18:30/0218 02:00
20020220 00:45/0220 12:00
20020222 11:15/0222 20:15
20020225 02:15/0225 08:30
20020227 06:00/0227 12:00
20020302 00:00/0302 03:15
20020306 10:00/0306 18:30
20020308 17:30/0309 06:00
20020311 02:15/0311 12:00
20020313 11:15/0314 00:15
20020316 04:45/0316 08:00
20020318 09:00/0318 14:45
20020320 20:30/0320 23:55
20020323 04:00/0323 09:45
20020327 23:45/0328 06:15
20020330 07:15/0330 12:45
20020401 19:30/0401 22:00
20020406 09:30/0406 18:00
20020408 15:00/0409 00:00
20020410 23:30/0411 09:45
20020413 08:30/0413 19:00
20020416 18:00/0417 04:30
20020418 06:00/0418 12:00
20020420 15:00/0420 23:00
20020422 20:00/0423 07:00
20020425 08:30/0425 18:00
20020430 04:40/0430 12:00
20020504 14:30/0504 16:45

Continued on next page

Table 3 – *Continued from previous page*

Start/End
20020505 02:30/0505 07:00
20020507 01:30/0507 15:45
20020508 11:00/0510 04:15
20020512 02:45/0512 09:30
20020514 10:30/0514 12:45
20020519 00:30/0519 19:30
20020521 01:30/0521 22:00
20020523 23:30/0524 02:00
20020524 19:00/0525 08:15
20020526 07:30/0526 10:30
20020528 20:00/0529 05:00
20020531 02:15/0531 13:30
20020602 04:30/0602 07:30
20020602 12:00/0602 21:30
20020604 08:30/0605 07:00
20020606 14:30/0607 16:30
20020609 06:00/0609 20:00
20020611 11:00/0612 13:00
20020614 01:00/0614 16:00
20020616 08:00/0616 18:00
20020620 13:30/0622 01:00
20020623 13:00/0623 17:00
20020624 04:00/0624 10:15
20020630 17:45/0701 15:00
20020701 21:00/0703 10:30
20020703 23:00/0706 03:15
20020707 01:00/0708 23:00
20020710 11:30/0714 03:30
20020714 15:45/0715 15:30
20020716 23:30/0717 16:00

Continued on next page

Table 3 – *Continued from previous page*

Start/End
20020718 05:45/0722 11:00
20020722 23:45/0728 01:00
20020728 02:00/0804 03:45
20020804 04:45/0811 06:15
20020811 07:30/0816 01:00
20020816 15:30/0818 09:00
20020818 10:00/0825 11:30
20020825 13:00/0901 14:15
20020901 17:15/0903 23:30
20020905 02:15/0906 16:30
20020907 10:30/0908 17:00
20020908 18:00/0915 19:30
20020915 21:00/0922 22:30
20020923 00:00/0923 23:30
20020924 03:30/0928 22:45
20020928 23:30/0930 01:00
20020930 02:15/1006 17:00
20021006 17:45/1007 03:30
20021007 05:00/1007 17:30
20021008 07:30/1010 22:00
20021010 22:30/1012 22:30
20021012 23:00/1014 06:30
20021014 09:00/1016 04:00
20021016 14:00/1019 00:15
20021019 01:30/1019 22:00
20021021 04:00/1022 19:30
20021022 22:30/1026 02:30
20021026 04:00/1029 20:15
20021030 01:30/1102 08:00
20021102 22:00/1104 22:00

Continued on next page

Table 3 – *Continued from previous page*

Start/End
20021106 00:00/1107 18:00
20021108 02:00/1109 18:45
20021111 00:00/1112 01:30
20021113 03:45/1114 14:15
20021115 20:30/1116 23:00
20021118 01:00/1118 23:30
20021120 17:00/1121 06:00
20021122 21:30/1124 01:00
20021125 04:00/1126 08:30
20021127 20:00/1128 18:30
20021130 04:00/1201 01:30
20021202 14:30/1203 09:00
20021204 22:00/1205 19:30
20021207 09:00/1207 16:30
20021207 18:00/1207 22:00
20021209 16:30/1210 14:30
20021212 13:45/1212 21:30
20021214 13:30/1214 20:00
20021214 21:00/1215 07:30
20021216 21:00/1217 15:00
20021219 08:00/1219 19:30
20021221 15:45/1221 23:15
20021222 00:30/1222 08:45
20021224 02:30/1224 14:00
20021226 10:00/1226 19:00
20021228 19:30/1229 02:30
20021229 04:00/1229 10:00
20021231 05:00/1231 18:45
20030102 12:30/0102 20:45
20030104 20:45/0105 06:00

Continued on next page

Table 3 – *Continued from previous page*

Start/End
20030105 07:00/0105 13:30
20030107 05:45/0107 21:00
20030109 17:00/0110 00:45
20030112 00:00/0112 09:15
20030112 10:30/0112 16:00
20030114 11:00/0114 20:00
20030116 20:30/0116 22:45
20030119 04:30/0119 09:30
20030119 14:00/0119 17:00
20030121 13:30/0121 21:30
20030126 07:30/0126 15:45
20030128 17:45/0129 08:15
20030131 01:30/0131 11:45

Start/End	OMNI			Cluster SC3			
	B_z [nT]	V_x [km/s]	P [cm $^{-3}$]	B_z	V_x	n_{CIS}	n_{EFW}
20020201 20:00/0203 04:00	-1.25	-373.52	4.08	y	y	n	y
20020211 13:00/0212 12:00	0.03	-533.11	2.18	y	y	y	y
20020218 09:00/0219 02:00	2.56	-362.41	3.46	y	n	n	y
20020219 06:30/0219 15:00	3.55	-401.63	1.25	y	y	n	n
20020220 18:30/0222 00:00	1.95	-440.18	1.96	y	y	n	y
20020318 17:30/0319 02:30	3.79	-429.30	15.34	y	n	n	n
20020412 20:30/0413 02:00	-1.81	-420.35	3.24	y	n	n	y
20021227 12:00/1228 03:00	0.09	-714.40	2.72	y	n	n	y
20021229 20:00/1230 16:00	-0.37	-526.40	2.26	y	y	n	n
20030106 06:00/0106 19:00	2.25	-399.91	1.50	y	n	n	n
20030108 07:00/0109 03:30	-0.58	-280.80	2.97	n	n	y	n
20030113 08:30/0113 18:00	0.68	-397.83	1.72	y	y	y	n
20030120 07:30/0120 13:00	2.16	-630.69	2.43	y	y	y	y
20030122 12:00/0123 14:00	0.13	-608.96	3.41	y	y	y	n
20030124 18:00/0126 00:00	-0.71	-739.68	2.87	y	y	n	n
20030127 16:00/0128 06:00	-0.92	-451.84	3.12	y	y	n	n
20030129 12:00/0130 18:00	-3.09	-450.00	3.96	y	y	n	y

1069 **Table 4.** The average OMNI input parameters in the solar wind and the good/bad agreement
 1070 of the GUMICS–4 simulations to the Cluster B_z magnetic field component, the V_x solar wind
 1071 speed component, the n_{CIS} solar wind density measured by the Cluster CIS HIA instrument and
 1072 the n_{EFW} solar wind density calculated from the spacecraft potential measured by the Cluster
 1073 EFW instrument in the solar wind.

Table 5: The average OMNI input parameters in the solar wind and the good/bad agreement of the GUMICS–4 simulations to the Cluster B_z magnetic field component, the V_x solar wind speed component, the n_{CIS} solar wind density measured by the Cluster CIS HIA instrument and the n_{EFW} solar wind density calculated from the spacecraft potential measured by the Cluster EFW instrument in the magnetosheath.

Start/End	OMNI			Cluster SC3			
	B_z	V_x	P	B_z	V_x	n_{CIS}	n_{EFW}
	[nT]	[km/s]	[cm $^{-3}$]				
20020201 13:30/0201 18:30	0.19	-342.87	4.62	y	n	n	n
20020208 18:15/0209 00:00	-0.48	-508.16	1.61	y	n	n	n
20020211 02:30/0211 09:00	-1.85	-425.67	1.78	y	y	y	y
20020212 16:30/0212 21:00	2.98	-509.22	2.34	y	n	n	n
20020219 17:30/0219 23:00	1.46	-431.50	1.46	y	y	y	y
20020222 23:00/0223 06:30	0.86	-391.22	1.14	y	n	n	n
20020227 16:30/0227 23:15	1.89	-343.13	1.52	n	n	n	n
20020310 18:30/0311 00:30	-2.81	-379.46	1.78	y	y	y	y
20020311 14:00/0311 19:00	1.63	-371.43	2.68	n	n	n	n
20020406 19:00/0407 01:15	-2.71	-333.13	0.93	y	n	n	n
20020410 17:30/0410 23:00	0.31	-312.43	4.42	n	n	y	y
20020411 11:30/0411 16:30	-1.50	-494.02	4.25	y	y	n	n
20020418 18:30/0418 22:45	-0.92	-450.82	0.30	n	n	n	n
20020421 04:30/0421 07:45	0.40	-455.69	1.37	n	n	n	n
20020422 11:45/0422 15:45	0.25	-419.98	1.14	n	n	y	y
20020423 08:30/0423 12:30	2.77	-507.99	6.82	n	n	n	n
20020430 12:30/0430 17:00	2.15	-479.51	3.02	n	n	n	n
20020505 07:00/0505 11:15	0.20	-336.81	1.74	n	n	n	n
20020506 19:15/0507 00:15	0.78	-390.00	2.46	y	n	n	n
20020507 17:30/0507 23:00	2.87	-392.40	3.49	y	n	n	n
20020514 22:45/0515 03:00	-2.42	-414.01	1.82	n	n	n	n

Continued on next page

Table 5 – *Continued from previous page*

Start/End	OMNI			Cluster SC3			
	B_z [nT]	V_x [km/s]	P $[cm^{-3}]$	B_z	V_x	n_{CIS}	n_{EFW}
20020517 07:00/0517 12:15	-0.39	-379.32	1.52	y	y	y	y
20020518 13:30/0518 19:30	0.63	-345.87	1.59	n	n	y	y
20020519 20:00/0520 03:30	4.75	-408.56	1.12	y	y	y	y
20020520 10:45/0520 20:15	0.74	-448.89	1.93	y	y	y	y
20020522 02:00/0522 08:45	-1.07	-398.12	1.63	n	y	y	y
20020527 02:15/0527 17:15	-3.11	-542.53	2.07	y	y	y	y
20020530 05:00/0530 10:30	0.03	-493.86	2.08	y	n	y	y
20020601 19:30/0602 01:00	-3.38	-342.27	4.16	y	y	y	y
20020602 21:45/0603 17:45	0.38	-435.47	1.89	y	y	y	y
20020605 10:30/0606 06:00	-0.42	-394.49	1.08	y	y	n	n
20020607 18:00/0607 22:00	-1.60	-291.85	1.80	y	y	y	y
20020608 01:15/0608 18:15	0.06	-335.39	2.74	y	n	y	y
20020610 01:30/0610 09:30	1.60	-465.52	3.00	y	y	y	y
20020610 11:00/0611 01:00	-2.27	-419.86	2.16	y	n	y	y
20020612 18:30/0613 06:15	-1.13	-351.03	1.16	y	y	y	y
20020615 07:00/0615 23:30	-1.16	-334.27	2.84	n	n	y	y
20020617 05:00/0618 03:45	0.78	-351.47	1.87	y	n	y	y
20020620 04:00/0620 11:00	0.46	-485.48	1.73	y	y	y	y
20020622 14:30/0622 18:00	-0.72	-429.02	1.93	n	n	y	y
20021201 04:15/1202 07:45	-1.09	-499.23	2.62	y	y	y	y
20021203 15:30/1204 19:30	0.34	-449.09	2.06	y	n	n	n
20021207 00:30/1207 07:45	0.80	-451.80	7.33	n	n	y	y
20021208 09:30/1209 08:00	0.60	-600.27	1.49	y	n	y	y
20021212 23:30/1213 14:30	0.10	-337.77	1.32	y	n	n	n
20021213 21:15/1214 09:30	-0.74	-361.19	2.99	y	n	y	y
20021215 12:45/1216 18:00	1.32	-479.48	1.53	y	n	n	n
20021217 16:30/1218 01:45	4.56	-393.99	2.49	y	n	y	y
20021220 01:30/1220 06:15	-1.21	-530.62	3.01	y	n	y	y

Continued on next page

Table 5 – *Continued from previous page*

Start/End	OMNI			Cluster SC3			
	B_z [nT]	V_x [km/s]	P $[cm^{-3}]$	B_z	V_x	n_{CIS}	n_{EFW}
20021223 02:15/1223 13:00	-2.32	-516.12	2.22	y	n	n	n
20021223 14:00/1223 22:30	0.89	-519.77	2.55	y	y	y	y
20021224 19:00/1225 01:45	0.88	-523.86	3.41	y	n	y	y
20021225 23:45/1226 07:15	-0.61	-414.38	2.21	y	y	n	n
20021226 23:00/1227 09:45	-1.79	-618.14	6.20	y	y	y	y
20021229 11:45/1229 17:00	-0.41	-580.12	2.39	y	n	n	n
20021230 17:45/1231 01:00	-1.01	-483.60	1.93	y	n	n	y
20021231 23:00/0101 05:15	0.60	-418.95	1.94	y	n	n	n
20030105 14:00/0105 21:00	-0.03	-414.46	1.69	y	n	n	n
20030106 23:15/0107 03:00	-1.62	-392.29	1.56	n	n	n	n
20030109 08:45/0109 16:15	1.45	-272.82	2.31	n	n	n	n
20030110 07:15/0110 15:15	-2.11	-401.03	2.72	y	n	y	y
20030111 08:15/0111 22:30	-0.20	-433.33	1.24	y	n	n	y
20030112 17:30/0113 00:15	1.53	-389.62	1.45	y	n	n	n
20030114 00:30/0114 08:30	-1.67	-388.53	2.27	y	n	n	y
20030116 10:15/0116 17:45	-1.20	-328.91	1.22	n	n	n	n
20030117 09:30/0117 13:30	-1.36	-327.09	2.55	y	y	y	y
20030118 23:30/0119 03:45	6.41	-459.46	4.82	y	y	y	y
20030119 21:00/0120 01:00	1.52	-597.95	2.38	y	n	y	y
20030121 06:30/0121 11:30	-1.77	-670.25	1.50	y	n	n	n
20030122 04:45/0122 09:30	0.11	-588.87	2.30	y	n	y	y
20030126 01:45/0126 06:30	-0.24	-713.82	2.75	y	y	y	y
20030127 08:15/0127 13:00	7.94	-509.30	0.47	y	n	y	y
20030128 12:30/0128 17:15	4.95	-443.83	4.15	y	y	y	y
20030130 19:45/0131 00:15	4.21	-510.33	2.63	y	n	y	y

Table 6: Intervals around the studied bow shock crossings. The Cluster SC3 crossed the bow shock in all cases. The 2nd column shows whether the bow shock is visible in the GUMICS–4 simulations.

Start/End	GUMICS Bow Shock
20020201 12:00/0202 00:00	+
20020203 00:00/0203 12:00	+
20020206 06:00/0206 18:00	+
20020208 18:00/0209 06:00	+
20020211 06:00/0211 18:00	+
20020212 12:00/0212 18:00	+
20020213 12:00/0213 18:00	+
20020216 00:00/0216 12:00	+
20020217 06:00/0217 12:00	-
20020218 06:00/0218 18:00	+
20020219 00:00/0219 18:00	+
20020220 12:00/0221 00:00	+
20020221 18:00/0222 00:00	+
20020301 06:00/0301 12:00	+
20020304 12:00/0304 18:00	+
20020306 00:00/0306 06:00	+
20020307 00:00/0307 06:00	+
20020308 06:00/0308 12:00	+
20020309 06:00/0309 12:00	+
20020310 12:00/0311 00:00	+
20020311 18:00/0312 00:00	+
20020313 00:00/0313 06:00	-
20020314 00:00/0314 12:00	+
20020316 06:00/0316 18:00	+
20020318 12:00/0319 00:00	+
20020323 12:00/0323 18:00	+

Continued on next page

Table 6 – *Continued from previous page*

Start/End	GUMICS Bow Shock
20020325 18:00/0326 06:00	–
20020327 06:00/0327 12:00	+
20020329 18:00/0330 00:00	–
20020402 00:00/0402 06:00	+
20020405 18:00/0406 00:00	–
20020407 00:00/0407 06:00	–
20020409 06:00/0409 12:00	–
20020410 12:00/0410 18:00	–
20020411 12:00/0411 18:00	–
20020413 00:00/0413 06:00	+
20020413 18:00/0414 06:00	+
20020420 00:00/0420 06:00	+
20020423 12:00/0423 23:00	+
20020427 00:00/0427 06:00	+
20020428 06:00/0428 12:00	+
20020430 18:00/0501 00:00	+
20020505 06:00/0505 18:00	–
20020507 18:00/0509 06:00	+
20020510 06:00/0510 12:00	+
20020513 12:00/0513 18:00	+
20020515 00:00/0515 06:00	–
20020520 00:00/0520 06:00	+
20020522 06:00/0522 12:00	+
20020522 18:00/0523 06:00	+
20021206 06:00/1207 06:00	+
20021218 00:00/1219 00:00	+
20021220 18:00/1221 00:00	+
20021221 00:00/1221 12:00	+
20021222 12:00/1223 00:00	+
20021223 00:00/1223 06:00	+

Continued on next page

Table 6 – *Continued from previous page*

Start/End	GUMICS Bow Shock
20021225 06:00/1226 00:00	+
20021227 06:00/1228 00:00	+
20021228 00:00/1228 12:00	+
20021229 12:00/1230 00:00	+
20030101 06:00/0102 00:00	+
20030103 06:00/0103 12:00	+
20030104 00:00/0104 18:00	+
20030106 00:00/0107 00:00	+
20030108 00:00/0108 12:00	+
20030113 00:00/0114 06:00	+
20030115 00:00/0115 12:00	+
20030118 18:00/0119 00:00	+
20030120 00:00/0121 12:00	+
20030122 06:00/0122 12:00	+
20030123 12:00/0124 00:00	+
20030124 12:00/0124 18:00	+
20030126 00:00/0126 06:00	+
20030127 00:00/0127 18:00	+
20030128 06:00/0128 18:00	+
20030129 06:00/0129 12:00	+
20030130 18:00/0131 00:00	+

Table 7: Intervals around the studied magnetopause crossings.
The Cluster SC3 crossed the magnetopause in all cases. The
2nd column shows whether the magnetopause is visible in the
GUMICS–4 simulations.

Start/End	GUMICS Magnetopause
20020203 06:00/0203 12:00	+
20020206 06:00/0206 12:00	-
20020211 00:00/0211 06:00	+
20020218 00:00/0218 06:00	+
20020225 06:00/0225 12:00	+
20020302 00:00/0302 06:00	+
20020306 18:00/0307 00:00	-
20020308 12:00/0308 18:00	-
20020311 12:00/0311 18:00	+
20020313 18:00/0314 00:00	-
20020314 00:00/0314 06:00	+
20020323 06:00/0323 12:00	+
20020330 12:00/0330 18:00	-
20020404 06:00/0404 12:00	-
20020409 00:00/0409 06:00	-
20020418 12:00/0418 18:00	+
20020422 12:00/0422 18:00	-
20020429 18:00/0430 00:00	-
20020507 12:00/0507 18:00	-
20020509 06:00/0509 12:00	-
20020510 00:00/0510 06:00	-
20020514 18:00/0515 00:00	-
20020519 12:00/0519 18:00	-
20020520 12:00/0521 00:00	-
20020522 00:00/0522 06:00	-
20020529 00:00/0529 12:00	-

Continued on next page

Table 7 – *Continued from previous page*

Start/End	GUMICS Magnetopause
20020530 06:00/0530 18:00	–
20020531 18:00/0601 00:00	–
20020602 18:00/0603 00:00	–
20020604 06:00/0604 12:00	–
20020605 06:00/0606 18:00	–
20020607 12:00/0608 06:00	+
20020609 00:00/0609 06:00	–
20020610 00:00/0610 06:00	–
20020611 00:00/0611 12:00	–
20020612 06:00/0614 00:00	–
20020614 18:00/0615 06:00	–
20020616 00:00/0616 12:00	+
20020620 00:00/0620 18:00	–
20020622 06:00/0622 18:00	–
20020704 12:00/0705 00:00	–
20020706 00:00/0706 12:00	+
20020709 00:00/0709 18:00	–
20020715 18:00/0716 12:00	–
20030105 06:00/0105 18:00	+
20030110 00:00/0110 12:00	+
20030112 12:00/0112 18:00	–
20030117 06:00/0117 12:00	+
20030121 06:00/0121 12:00	+
20030122 00:00/0122 06:00	–
20030126 18:00/0127 00:00	+
20030128 12:00/0128 18:00	+
20030129 00:00/0129 12:00	+
20030131 12:00/0201 00:00	+

Start/End	GUMICS Neutral Sheet
20020901 19:00/0902 00:00	–
20020906 14:00/0906 16:30	+
20020913 17:30/0913 20:00	+
20020918 13:00/0918 14:30	–
20020920 20:30/0921 02:00	+
20020928 03:00/0928 07:00	+
20021002 16:00/1003 00:00	–
20021014 12:30/1014 23:00	+
20021017 03:00/1017 04:00	–

1077 **Table 8.** Intervals around the studied neutral sheet crossings in the tail. The Cluster SC3
 1078 crossed the neutral sheet in all cases. The 2nd column shows whether the neutral sheet is visible
 1079 in the GUMICS–4 simulations.